Delft University of Technology

Exploring the Impact of Micro-environment Changes in Hybrid Molecular Catalyst Systems on CO_2 Electrochemical Reduction Beyond CO

Master of Science Thesis

Juan José Castro Villagómez

Main Supervisor:	Dr. Thomas Burdyny
Daily Supervisor:	Dr. Jasper Biemolt
Committee Members:	Dr. Arjan Houtepen
	Dr. Rienk Eelkema

Project Duration:	September, 2023 - June, 2024
Place:	Faculty of Applied Sciences, Delft
Student Number:	5710375

Acknowledgement

I would like to express my gratitude to my committee members **Arjan Houtepen** and **Rienk Eelkema** for accepting being part of my committee and for taking the time to read my report.

To **Tom**: I will always be grateful for the opportunity to join the Burdyny Energy Lab. Thank you for your guidance, the scientific discussions, and for keeping your door open to any crazy idea that passed through my head. Thank you for believing in me. You are a great leader, Tom, and your work inspires many young researchers to believe we can all take part in making a positive change in our world.

To **Jasper**: Coach, thank you for believing in me and pushing me to my limits, helping me prove to myself that I can reach my goals. Your critical feedback when I needed it, and your support and understanding when I most needed it, have been invaluable. Thank you for always guiding me to find answers to my own questions with just a little "push." Your guidance, advice, and perspective have set an example that I will always keep and apply to many aspects of my life. You are a great mentor, and your ways of explaining difficult concepts through stories have inspired me. Thank you for your patience and invaluable lessons!

To **Hugo**, **Sid** and **Jesse**: Your motivation is inspiring and reflects the great researchers you are. Thanks for all the advice, coffees, and help throughout the project!

To **Joost**, **Herman**, **Lars**, and all the other members of MECS: Your willingness to help and engage in discussions has been of great support, and I will always be thankful for that.

To my friends, who have supported me through every step of this journey and have made the sky in Delft much brighter than what the clouds show.

To my cousin **Greg**, who has heard my crazy thoughts about my thesis for 9 months and has cared for me and supported me more than anyone else.

And to **my family**, whom I miss the most in the world, and who have supported me and granted me the opportunity to follow my dreams. This thesis is dedicated to you.

I believe together we can make an impact in making our world a little brighter, a little greener, and a little better than how we found it.

With much love,

Juan José

Contents

List of Figures

Abstract

Our world has witnessed the devastating effects of fossil fuels extraction; the primary energy source for modern society. Transitioning to sustainable energy sources requires exploring alternative fuel production methods, focusing on utilizing captured anthropogenic CO_2. Electrochemical reduction of CO_2 (CO_2RR) using renewable electricity presents an attractive option for storing energy in chemical bonds. While many electrocatalysts efficiently reduce CO_2 to CO, only a few, such as copper, can produce high energy-dense molecules like ethanol or methanol with selectivities exceeding 60%. Molecular catalysts (MCs) hold promise as alternatives to metallic electrocatalysts, particularly when immobilized on the surface of gas diffusion electrodes (GDEs), where state-of-the-art CO_2RR takes place. However, their efficiency and scalability must be addressed for industrial applications. Our work focuses on evaluating the impact of engineering the micro-environment at the interface where CO_2RR occurs, for the purposes of optimizing the performance of MCs systems.

Specifically, the electrode active-site interaction for the CO_2-to-ethanol pathway was investigated using a nickel iron-tetraphenylporphyrin (Ni-FeTPP) electrocatalyst. We explored the challenges of translating a molecular catalyst system from an unconventional 3D electrode design to a GDE-based electrolyzer. The difficulty lies in replicating the strong electronic coupling between Ni and FeTPP necessary for enabling the CO_2-to-ethanol pathway; which led to two methods of coupling Ni to FeTPP: drop-casting and spray-coating. Although our system did not achieve CO_2 reduction to ethanol, it provided significant insights into the impact of subtle micro-environment changes. These changes uncovered possible unintended interactions, suggesting the formation of nickel hydride species that could greatly influence the CO_2-to-ethanol pathway catalyzed by Ni-FeTPP. Moreover, the competing behavior between CO_2 and CO to enhance the CO_2-to-methanol pathway was adressed by using cobalt phthalocyanine supported on multi-walled carbon nanotubes (CoPc/MWCNT). We engineered the local environment where molecular catalysts interact by introducing silver nanoparticles and PTFE particles to increase local CO availability near the active sites and promote further CO reduction. This approach resulted in a remarkable 4-fold and 17-fold increase in the Faradaic efficiency of methanol, from the addition of silver nanoparticles and PTFE particles, respectively. Our results demonstrate the CO_2-to-methanol pathway is enhanced through the modification of the catalyst surface micro-environment of the GDE. Our research contributes to a deeper understanding of the prospect for improving the challenging electrochemical reduction of CO_2 beyond CO.

1 Introduction

The need for long-term energy storage has become central as the world's economy transitions towards sustainable energy practices. Storing this energy by housing renewable electrons in the form of chemical bonds has become a promising and carbon-neutral solution.[1] Furthermore, integration with anthropogenic CO_2 capture technologies will accelerate the transition from fossil-based fuels and feedstock chemicals to carbon-neutral alternatives.[2] Nevertheless, the use of recovered CO_2 needs to be optimized before it can be implemented on a global scale.

In this pursuit, electrochemical pathways powered by green electricity have demonstrated intrinsically smaller carbon footprints when compared to other energy-intensive thermochemical routes.[3] Hence, significant efforts have been directed towards developing pathways for the electrochemical reduction of carbon dioxide (CO_2RR) at industrially relevant current densities (>200 $mA\ cm^{-2}$).[4] Therefore, reaching economically-feasible CO_2 conversion rates significantly depends on the catalytic surface where CO_2RR takes place. Consequently, for this technology to be further developed and implemented, it is essential to fundamentally study effective electro-catalytic materials together with their effects on the CO_2RR local environment.[5]

1.1 Current State-of-the-art CO_2RR

The challenge of electrocatalysts for CO_2RR is that they must overcome the high thermodynamic stability of the CO_2 molecule. This results in a high activation energy required to carry out the reaction under near-ambient conditions.[6] Therefore, electrocatalysts play a crucial role in facilitating CO_2RR by minimizing the activation energy required for the reaction to proceed. This leads to a lower overpotential required to drive CO_2RR at significant rates, which is necessary to compete against the more thermodynamically favorable hydrogen evolution reaction (HER).[5,7] Therefore, exploring highly active, selective, and cost-effective electrocatalysts that can be applied to systems with promising scalability emerges as an appealing alternative.

To address this need, scalable CO_2 electrolyzers incorporate the use of electrocatalysts onto gas diffusion electrodes (GDEs). A growing body of evidence continues to prove that GDEs can achieve increased reaction rates, and therefore higher product yields.[8] This is due to their ability to overcome the low solubility of CO_2, which restricts the highest attainable CO_2RR current density when compared to aqueous H-cell type electrolyzers.[9] The focus has therefore centered on incorporating electro-catalytic materials into the GDE catalyst layer (CL) to achieve higher current densities with high product selectivity.

Most CO_2RR related research revolves around metallic catalysts such as Ag and Au for CO_2-to-CO or Sn for formate production.[10] For higher C_{2+} products, Cu is the primary option, yielding a broad spectrum of products such as methane, ethylene and ethanol, among others.[11] However, such a product mix gives separation issues downstream, making Cu CO_2RR less attractive.[12] To enhance product selectivity we require alternative electrocatalysts with well-defined but tailorable active sites.

1.2 Molecular Catalysts and Hybrid Systems for CO_2RR

This is especially true for molecular catalysts (MCs), which are metal-organic structures designed for specific catalytic reactions. These catalysts achieve high reactivity and selectivity in CO_2RR through the interaction of their interchangeable metal center and tunable ligands.[13] MCs mediate CO_2RR by accepting an electron from the electrode surface and donating it to the CO_2 in solution in a 2-phase boundary reaction.[14] CO_2 then undergoes further reduction in multi-electron multi-proton steps as the MC reduces back to its original oxidation state.[15] The key advantage that makes MCs unique for CO_2RR— compared to metallic catalysts—is their ability to modify their electronic structure, which changes the binding strength of CO_2RR intermediates.[16]

Nevertheless, most experimental work on MCs for CO_2RR has been restricted to the scope of mass-

transport-limited homogeneous reactions. Recent developments however, have advanced the study of immobilization of MCs on the catalyst surface of GDEs by the use of different support materials, which create hybrid heterogeneous systems.[17] These hybrid systems benefit from the unique reaction mechanisms of MCs, while also allowing for the manipulation of their active sites and supports. Heterogenization of molecular complexes has been shown to achieve elevated reaction rates due to highly dispersed catalysts, which require less material and increase the number of electrochemically active sites. Consequently, hybrid MCs have proven to be advantageous for CO_2RR when compared to their homogeneous counterparts.[13]

Hybrid systems have given way to fundamental research into their reaction mechanisms and interactions with supports during CO_2RR. Recent studies have revealed that MCs can exhibit a strong electronic coupling with certain support materials.[18] This robust interaction situates them within the electrical double layer (more specifically the outer Helmholz plane or OHP) at the surface-liquid boundary during an electrochemical reaction, significantly altering their behavior. A key feature is the sustained oxidation state of the metal center during the electron transfer processes. This leads to non-redox-mediated electrochemical reactions that have been proven to enhance the selective behavior of MCs.[19]

The features of hybrid MCs, including the ability to tune the metal center and ligands, as well as the methods of immobilization—whether through covalent bonds or non-covalent interactions—have demonstrated to enhance their electro-catalytic properties for CO_2RR.[20] These versatile characteristics of MCs inspire further investigation into their potential to achieve high faradaic efficiencies (FEs) for CO_2-to-CO conversion and beyond, to reduce the overpotential of the CO_2RR, and to attain industrially relevant product current densities exceeding 200 $mA\ cm^{-2}$.

However, while most MCs exhibit high selectivity for CO_2-to-CO or formate, a select group of MCs has proved capable of attaining reduction towards C_{2+} products; these include metallo-porphyrins and metallo-phthalocyanines which are currently being studied in hybrid systems. Although the rates at which they produce higher carbon products are not yet suitable for industrial applications, their ability to go beyond CO makes them an attractive competitor to metallic catalysts.[21] Yet, not only their reaction mechanism needs to be fundamentally understood, also the effects in local pH, wetting of the catalyst layer, concentration of reactants and intermediates as well as their binding strengths to the active sites. All these challenges—or opportunities—make hybrid MCs 'puzzling' to study.[8]

Nevertheless, to achieve the further reduction of CO_2 beyond CO by Hybrid MCs, it is important to understand and piece together every component of this selectivity 'puzzle', which includes the local environment interaction, and the electrode-active site interaction (Fig.1b).

1.3 CO_2RR beyond CO

To further understand the principle under which CO_2RR beyond CO happens, the strength of the metal-CO adduct is a key parameter. Following the Sabatier principle, a strong *CO adduct reacts only at high overpotentials, where HER predominates, while a weaker bond will desorb from the surface.[22] Therefore, a moderate binding energy (BE) is needed to keep *CO bound to the catalytic site for its further multi-electron reduction with a reasonably low energy barrier. Hence, MCs that meet this requirement are considered for the task.[23]

A recent study conducted by Li *et al* explored a hybrid system integrating iron-tetraphenylporphyrin (FeTPP) by a non-covalent immobilization onto carbon nano-tubes (CNT)[24]. The study successfully demonstrated the translation of FeTPP, mostly studied in H-cells, onto a GDE-based electrolyzer; attaining a $FE_{CO} > 60\%$ across a broad potential range, starting from -0.41 V_{RHE}. More interestingly, when this MC was integrated onto a copper-sputtered GDE, it achieved a notable $FE_{ethanol}$ of 41% and a corresponding partial current density ($j_{ethanol}$) = -124 $mA\ cm^{-2}$ at -0.82 V versus RHE, while Cu by itself only reached a $FE_{ethanol}$ = 27% and $j_{ethanol}$ = -65 $mA\ cm^{-2}$. This case emphasizes the significance of increasing the local concentration of CO, which serves as a key intermediate for

carbon–carbon coupling reactions. Moreover, it underscores the promising opportunities presented by hybrid systems in enhancing selectivity beyond CO.

Another MC that has shown remarkable CO_2-to-CO and notable C_{2+} activity in hybrid systems is Cobalt Phthalocyanine (CoPc). The onset potential for CO_2-to-CO conversion is observed when CoPc undergoes the $Co^{2+/1+}$ couple, reported at -0.59 V_{RHE}.[25] A study by Zhang *et al.* evaluated CoPc supported on carbon nanotubes (CoPc/CNT), achieving a FE_{CO} of 97% with a current density of -200 $mA\ cm^{-2}$ at -0.8 V_{RHE}, making it one of the best-reported CO_2-to-CO electrocatalysts.[26] This low cathodic potential is notable as CoPc has shown CO_2-to-methanol activity at potentials more positive than -0.9 V_{RHE}. Research on CoPc has demonstrated an effective CO_2-to-methanol conversion pathway, influenced by the type of support and local CO_2 concentration.

However, few studies have reported promising FE_{CH_3OH} values. The interaction of the local environment is crucial for enhancing selectivity in hybrid CoPc electro-catalytic systems. When immobilized on carbon supports, CoPc demonstrates increased activity for CO_2RR through non-covalent $\pi - \pi$ interactions between the π electron clouds of adjacent aromatic groups in the CoPc structure.[25] A study by Su *et al.* showcases one of the few successful 6 electron-6 proton CO_2-to-CH_3OH reduction on a flow cell by monodispersed CoPc/CNT on a carbon-GDE.[27] The report shows a FE_{CH_3OH} of 31.3% with a methanol partial current density (j_{CH_3OH}) of -66.8 mA cm^{-2} at -0.93 V_{RHE}. By performing CO reduction, the results reached a FE_{CH_3OH} of 50.5% and a j_{CH_3OH} of -62.1 mA cm^{-2} at -0.8 V_{RHE}. These findings demonstrate the possibility of enhancing selectivity beyond CO by inducing molecular distortions to the MC through their local interaction with CNT.

Nevertheless, understanding the mechanism of hybrid interactions and roles of every component of the micro-environment phenomena adds both complexities and opportunities to the design and optimization of hybrid systems. Hence, addressing this challenge promises compelling developments in the context of CO_2RR.

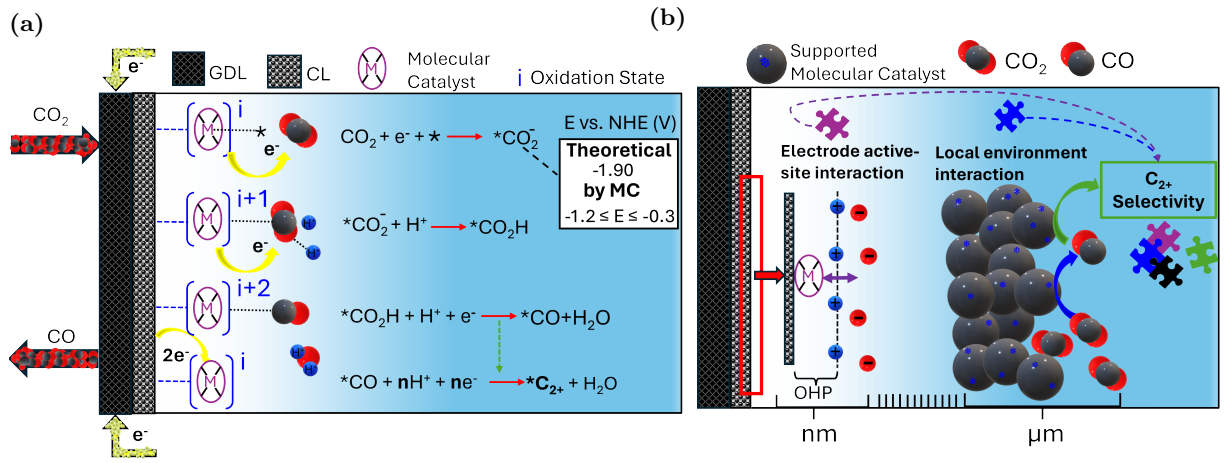

Figure 1: **(a)** CO_2RR mechanism by an immobilized molecular catalyst on a GDE.[28] The thermodynamic barrier of the reaction rests upon breaking the C=O bond and the stable linear geometry of the CO_2 molecule. This represents a high theoretical electrode potential (-1.9 V vs NHE) required to carry on the reaction without an electro-catalyst. Hence, IMCs can decrease the activation energy required for the reaction, allowing it to proceed at lower overpotentials necessary to drive CO_2RR at significant rates, with the possibility of further reducing CO.[16]
(b) The interaction between the immobilized MC and the electrode within the electrical double layer (Outer Helmholtz Plane - OHP), and the influence of the local environment where the MC interacts with CO/CO_2 molecules are two key parameters to piece together the selectivity 'puzzle'.

Taking into account the aforementioned cases and extensive phenomena involved, addressing the challenging CO_2-to-C_{2+} mechanism requires careful consideration of electrode active-site interactions and local environment (Fig.1b). To enhance selectivity for C_{2+} products, the research focus in this work is directed towards hybrid MCs within the catalyst layer of the GDE. This prompts the following

research question:

How can changes in the micro-environment of the GDE's (hybrid) molecular catalyst layer enhance the selectivity of CO_2RR beyond CO?

2 Experimental

2.1 Cathode Gas Diffusion Electrodes Fabrication

Metallic nickel layers were deposited directly on carbon gas diffusion layers (GDLs) (Sigracet 39BB®) via DC magnetron sputtering to form a 300 nm layered nickel gas diffusion electrode (Ni-GDE) (2 cm x 2 cm); and silver metallic layers were deposited on expanded polytetrafluoroethylene (ePTFE) GDLs (3 cm x 3 cm) following the same sputtering procedure, to form 100 nm layered Ag-ePTFEs. Molecular catalyst deposition followed on the GDEs via i) drop-casting or ii) spray deposition.

i) **Drop-casting procedure: Ni-FeTPP electrodes** (Fig.2a): 0.128 mg of Commercial 5, 10, 15, 20-Tetraphenyl-21H,23H-porphine iron (III) chloride (Sigma-Aldrich) were dissolved in 1 mL of dichloromethane (DCM) HPLC grade (Fisher Scientific) and was subjected to ultrasonication for 20 minutes. This was followed by drop-casting 250 μL of the resulting solution directly onto the Ni-GDE (effective area of 2.25 cm^2) using a 1000 μL micro-pipete, aiming for 0.0142 $mg\ cm^{-2}$ loading (A.1). The higher loadings (1.4, 2.8 and 6.5 $mg\ cm^{-2}$) were prepared based on the same proportions. The resulting electrodes were dried in a vacuum oven at 50°C for 16 hours.

ii) **Spray-deposition** (Fig.2b):

- **Ni-FeTPP on carbon GDEs:** 15 mg of Nickel nanopowder (< 100 nm average particle size, Sigma-Aldrich) was suspended in 15 mL of high-purity 2-propanol (HPLC grade, Fisher Scientific) and mixed with 7.68 x 10^{-5} mg of FeTPP (A.2) achieved by subsequent dilutions in 2-propanol. The mixture was then subjected to ultrasonication for 20 minutes in an ice bath. Then, 25 μL of Nafion® perfluorinated resin solution (Sigma Aldrich) was added to the catalyst ink and ultrasonicated again for 20 minutes in an ice bath. Spray-deposition followed by loading 5 mL of the catalyst suspension on the automated air-brush to proceed with spray-coating the carbon GDE. The automated air-brush had an incorporated heating plate set at 80 °C. The resulting Ni-FeTPP electrodes surface loading was calculated between 0.4-0.6 $mg\ cm^{-2}$ and dried in a vacuum oven at 50°C for 16 hours.
- **CoPc/MWCNT on Ag-ePTFEs:** 10 mg of Multiwalled carbon nanotubes (MWCNT) (Sigma Aldrich) were mixed together with 0.3 mg of Cobalt (II) Phthalocyanine (CoPc) (3 wt% ratio) and suspended in 10 mL of 2-propanol. This suspension was subjected to ultrasonication for 30 minutes in an ice bath. After which 100 μL of Nafion solution (Sigma Aldrich) was added and ultrasonicated again for 30 minutes in an ice bath. Two mL of the resulting base-case suspension were spray-deposited onto the Ag-ePTFEs using an automated air-brush with an incorporated heating plate set at 60 °C. The resulting CoPc/MWCNT electrodes surface loading was calculated between 0.3-0.5 $mg\ cm^{-2}$. For the modified CoPc/MWCNT electrodes, additional silver nanoparticles (+20wt% = 1.5 mg) and PTFE water-based solution (+50 wt% = 5 μL) containing particles < 200 nm (Sigma Aldrich) were added to the base-case catalyst suspension and ultrasonicated for 30 minutes as an intermediate step prior to the addition of 100 μL of Nafion® binder. This followed the same spray-deposition procedure on the Ag-ePTFEs.

2.2 Electrochemical Measurements

The electrochemical experiments were applied using either a Princeton Applied Research® Parstat 4000 (±48 V, 20 A) or MC-1000 (±12 V, 2 A), in a three-electrode configuration. Potentiostatic EIS measurements were performed twice at the beginning of each experiment to determine the resistance of the cell to proceed with the IR corrections. After, cyclic voltammetry (5 cycles) measurements were done at a scan rate of 100 mV s^{-1} for every experiment. This followed either chronoamperometry or chronopotentiometry experiments. All potentials were measured against the reversible hydrogen electrode (V_{RHE}). *For the chronopotentiometry experiments using Ag-based electrodes is important

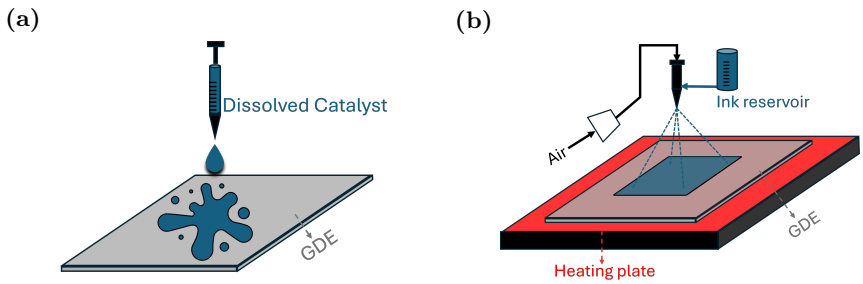

Figure 2: Catalyst deposition methods on GDEs via **(a)** Drop-casting and **(b)** Spray-coating.

to finalize the analysis after going back to open circuit potential (OCP) as we detected that by doing so, the catalytic activity gets compromised (see A.18).

2.3 Flow Cell set-up

Both catholyte and anolyte used in each experiment was 0.5M $KHCO_3$. A HydroFlex® reversible hydrogen electrode (RHE) was used as the reference electrode. Sustainion® Grade 60 anion exchange membranes (AEM) were used. The current collectors for Ag-ePTFE cathodes were copper-tape based, precision-plotted using a Cricut® Maker 3.

i) **Ni-FeTPP experiments conditions:** A platinum mesh was used as the anode. Both catholyte and anolyte flow-rates were fixed at 10 $mL\ min^{-1}$. CO_2 flowrate was fixed at 10 sccm. The effective electrochemical area of this set-up was fixed at 2.25 cm^2.

ii) **CoPc/MWCNT experiments conditions**: An iridium oxide electrode was used as the anode. Both catholyte and anolyte flow-rates were fixed at 20 $mL\ min^{-1}$. The CO_2 flowrate was maintained at 5 sccm and mixed together with 3sccm of N_2 at, giving a total 8sccm gas inlet. The effective electrochemical area of this set-up was constant at 5 cm^2.

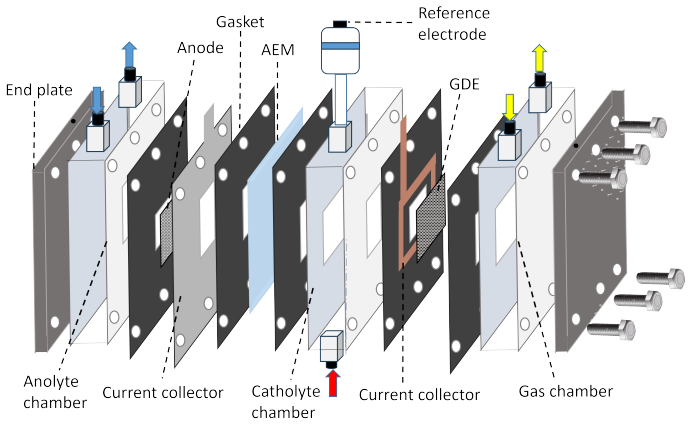

Figure 3: Flow-cell design used throughout the project. AEM: Anion exchange membrane, GDE: Gas diffusion electrode

2.4 Products Analysis

Liquid Products: All liquid products were analyzed via H-NMR. For the preparation of the samples, 500μL of our liquid products were mixed with 50 μL of a 4mM DMSO solution and 50 μL of deuteriom oxide. This was followed by vortex-mixing to ensure homogenization prior to analysis.

Gas Products Analysis: Gases produced during experiments were analyzed via in-line Gas Chromatography, GC Global Analyser Solutions® CompactGC 4.0. For Faradaic efficiency estimation see A.3.

3 Results and discussion

We explored two case studies to evaluate the effect of engineering the micro-environment of hybrid molecular catalysts on GDE-based electrolyzers for CO_2RR. The first case study examined electrode active-site interactions through the electrochemical reduction of CO_2-to-ethanol using a nickel-iron tetraphenylporphyrin (Ni-FeTPP) electrocatalyst. The second case study briefly explored the local environment interaction as a *proof-of-concept* through CO2-to-methanol reduction via CoPc supported on multi-walled carbon nanotubes (MWCNT). Both case studies have helped us gain deeper understanding on the challenging reduction of CO2 beyond CO.

3.1 Electrode-active sites interaction: Ni-FeTPP for CO_2-to-ethanol

The effect of electrode active-site interaction was recently demonstrated in a study by Abdinejad *et al.*, where CO_2-to-ethanol was catalyzed by a Ni-FeTPP electrode.[29] The study used a gas-fed electrolyzer with a Ni 3D electrode with drop-casted FeTPP used as the cathode. This set-up achieved a $FE_{ethanol}$ = 68% and a total current density of -31 $mA\ cm^{-2}$ at -0.3 V_{RHE} in 0.5M $KHCO_3$ media. These results outperform Cu electrocatalysts in terms of ethanol selectivity and by-product formation.

The authors suggested that the CO_2-to-ethanol reduction is a result from the strong electronic coupling between Ni and the FeTPP structure. Such interaction places the MC inside the electrochemical double layer (more specifically within the outer Helmholtz plane or OHP), sustaining the oxidation state of the metal center throughout the redox event.[19] This strong Ni-FeTPP coupling fixes the oxidation state of Fe between $Fe^{3+/2+}$, preventing the characteristic CO release reported at an Fe^{1+}state.[30]

However, this system was based on an unconventional 3D electrode design rather than a GDE-based electrolyzer. Adapting to a GDE-based system aims to overcome mass-transport limitations, as GDEs are known to enhance reactant delivery to the catalyst. Additionally, GDEs allow for more fundamental studies as research infrastructure grows for GDE-based electrolyzers. Nevertheless, this transition is challenging because the phenomena involved in CO_2RR may differ between the two systems. Factors like the different dimensional scales of the electrodes, ensuring strong electronic coupling between Ni and FeTPP, the delivery of CO_2 to the catalytic surface, and the effect of the competing HER contribute to the complexity of this transition. Ultimately, preparing this catalyst on a GDE would facilitate translation to industrial conditions (Fig.4), but it would also alter the crucial local microenvironment.

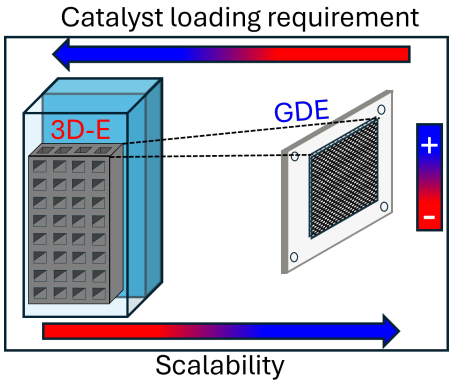

Figure 4: Translation of the Ni-FeTPP interaction in a 3D electrode onto a gas diffusion electrode (GDE), motivated by the prospect of higher scalability and lower catalyst loading requirement.

3.1.1 Translating the Ni-FeTPP interaction into a GDE-based flow-cell

To accomplish the translation of the Ni-FeTPP interaction from a 3D electrode to a GDE, nickel was sputtered on carbon GDEs (C-GDEs) to obtain a 300 nm layer (Ni-GDE). The same drop-casting procedure of FeTPP done by Abdinejad *et al.* was followed to ensure the proper translation into the Ni-GDE to use it in a flow-cell set-up.[29] FeTPP loading was calculated based on the Ni content of the 3D electrode (3wt%), which resulted in areal loading of 0.0142 $mg\ cm^{-2}$ over the Ni-GDE (A.1).

The electrochemical behavior of the system was evaluated by comparing the blank (Ni-GDE) and the Ni-FeTPP electrode (Fig.5).

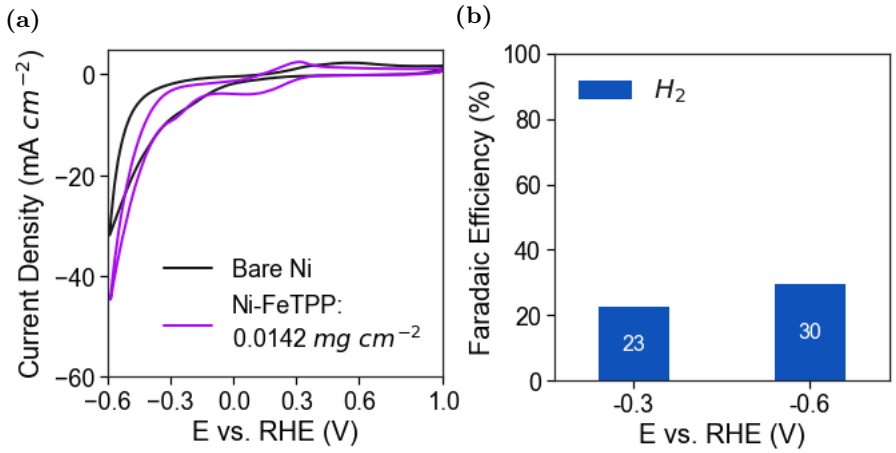

Figure 5: **a)** Cyclic voltammogram of Ni sputtered on a C-GDE (Bare Ni) and FeTPP drop-casted on a Ni-GDE with an areal loading of 0.0142 $mg\ cm^{-2}$ under CO_2 atmosphere **b)** Faradaic efficiencies for the Ni-FeTPP electrode calculated after 30 min of chronoamperometry at different reductive potentials under CO_2 (A.3).
*The system's inability to reach 100% FE is attributed to the low current densities, which amplify the impact of possible side reactions on the total FE. As the potential becomes more negative, a higher FE_{H_2} is reached as HER becomes more predominant.[31]

The Ni-FeTPP cyclic voltammogram (Fig.5a) suggests that FeTPP undergoes a redox process. We observe this in the additional redox couple at 0.3 V_{RHE} assigned to the $Fe^{3+/2+}$couple of FeTPP when comparing it to the bare Ni curve.[32] This indication that FeTPP is undergoing a redox process suggests that it has not achieved a strong electrode active-site interaction. The peak located at -0.3 V_{RHE} for both bare Ni and Ni-FeTPP (Fig.5a) is attributed to the $Ni^{2+/0}$couple and is explained more in detail for the bare Ni behavior in A.2.

No CO_2RR products were detected after 30 minutes of electrolysis at -0.3 and -0.6 V vs.RHE (Fig.5b). These results differ from Abdinejad *et al.* where ethanol production reached its optimum at -0.3 V_{RHE}, following a non-redox mediated electro-catalytic process.[29] This is important because pure FeTPP has not been reported to be active for a redox-mediated CO_2RR at -0.3 V_{RHE}.[33] In fact, the onset potential for CO_2-to-CO catalyzed by immobilized FeTPP is indicated at -0.41 V_{RHE} and is assigned to the $Fe^{2+/1+}$couple.[30] Thus, our initial results indicate that:

1. Ni-FeTPP did not achieve a strong electronic coupling as no ethanol was detected in the liquid products.
2. FeTPP on our electrode's surface is not electrochemically active for CO_2RR at a potential of -0.6 V_{RHE} where it is reported to be active.

Following this, we hypothesize the Ni-FeTPP interaction may have been limited due to the low FeTPP loading on the Ni-GDE. Consequently, the limited active sites on the surface may not be sufficient for significant CO_2RR activity to be detected at a loading of 0.0142 $mg\ cm^{-2}$. This, along with FeTPP's potential to leach or dissociate from the surface after sustained contact with the electrolyte,

provides an insight as to why there is the lack of CO_2RR activity while showing initial redox activity for FeTPP's metal center during cyclic voltammetry.

To further prove this hypothesis, we tested higher loadings. We determined a reasonable loading, by considering the penetration depth of drop-casted FeTPP onto the GDE. Note that the sputtered Ni layer is only 300 nm, while the GDL of the GDE has a total depth of 325 μm. This three-order of magnitude difference indicates the scale at which we should load our GDE, acknowledging that not all material will remain on the Ni surface. To avoid overloading our GDL, we chose a reasonable two-order magnitude increase from the initial 0.0142 $mg\ cm^{-2}$. This resulted in loadings of 1.4, 2.8, and 6.5 $mg\ cm^{-2}$ of drop-casted FeTPP onto the Ni-GDE to ensure significant Ni-FeTPP interaction across the entire electrode surface (Fig. 6a).

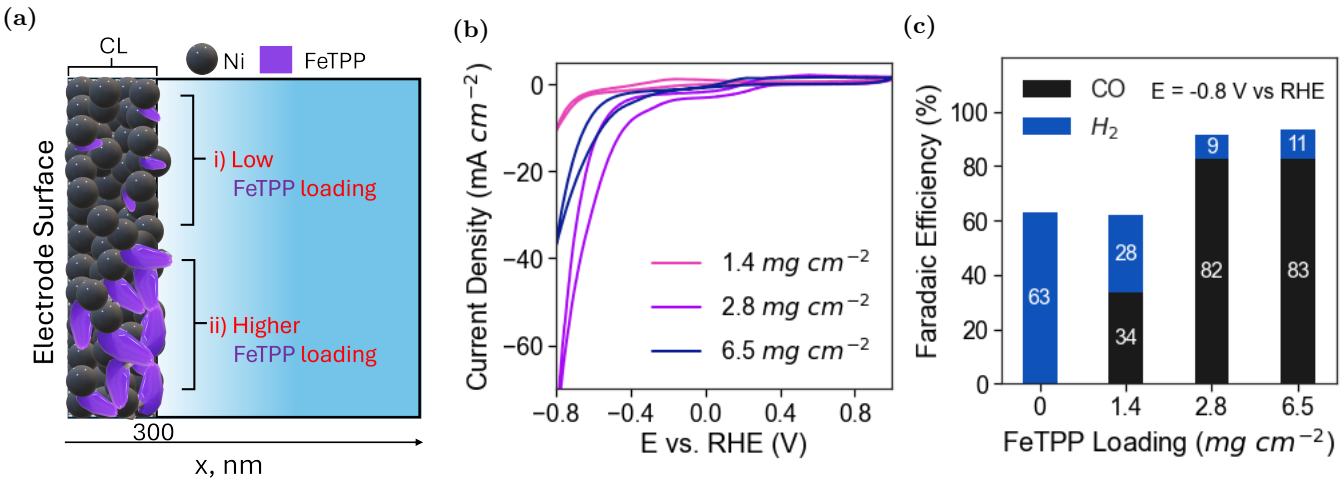

Figure 6: **a)** Comparison schematic of different FeTPP loadings on the Ni catalyst layer. Behaviour of different FeTPP loadings drop-casted on Ni-GDE under CO_2 atmosphere. **b)** Cyclic Voltammetry. **c)** Faradaic Efficiencies calculated after 30 min of chronoamperometry at a reductive potential of -0.8 V_{RHE} (A.4).

Ethanol would be detected at -0.3 V_{RHE} if the desired strong electronic coupling between Ni and FeTPP were achieved by eliminating the redox-mediated CO_2RR. If this is not the case, the redox interaction (Fe^{2+}/Fe^{1+} couple) enabling *CO desorption from the active site would be expected at more negative potentials. Therefore, the potential range for the electrochemical measurements of the higher loadings presented in Fig.6 was extended to -0.8 V_{RHE}.

Ethanol was not detected in the liquid products during 30 minutes of electrolysis at different reductive potentials (-0.3, -0.4, -0.6, -0.8 V_{RHE}). CO, however, was detected at -0.4 V_{RHE} for the higher FeTPP loadings and showed the highest FE_{CO} at -0.8 V_{RHE} (Fig.6c). This is consistent with FeTPP's onset potential for CO_2-to-CO reported by Smith *et al.*[30]
Interestingly, the 2.8 and 6.5 $mg\ cm^{-2}$ loadings showed a similar behavior, suggesting a pseudo-optimal point at 2.8 $mg\ cm^{-2}$ due to the lower FeTPP loading required to reach a similar selectivity ($FE_{CO} = 82\%$, $FE_{H_2} = 9\%$). Additionally, longer chronoamperometry runs were done to ensure that the intended CO_2-to-ethanol pathway is not electrochemically dependent on time (A.6). Still, no ethanol was detected at -0.5 V_{RHE} even after 140 minutes of electrolysis.

The inability of our Ni-FeTPP electro-catalyst to reduce CO_2-to-ethanol is traced down to catalyst aggregation, which results in localized accumulation, uneven catalyst distribution and restricted interaction directly with the Ni surface. MCs are known for their inherently low conductive properties, which consequently limit the total number of electrochemically active sites due to aggregation, as also observed by Ren *et al.*[34] This hypothesis would also explain the low current densities achieved during the chronoamperometry runs (A.4).

To prove this low conductive behavior due to catalyst aggregation, we drop-casted the pseudo-optimum

loading of 2.8 $mg\ cm^{-2}$ directly onto a carbon GDE. This resulted in a lower CO_2-to-CO activity as compared to the Ni-FeTPP catalyst, as Ni is a more conductive substrate than carbon (A.5).

Reflecting on the results of testing higher FeTPP loadings on the Ni-GDE (Fig.6a & b), we can conclude three main points:

1. Ethanol was not detected in a potential range from -0.3 to -0.8 V_{RHE}.
2. CO was produced at a potential where FeTPP is known to electrochemically reduce CO_2-to-CO through a redox process (-0.8 V_{RHE}).
3. Possible catalyst aggregation is not ensuring the desired Ni-FeTPP strong electronic coupling.

To confirm the suspected catalyst aggregation and uneven FeTPP distribution across the Ni-GDE, the surface morphology of the blank (Ni-GDE) and the pseudo-optimum 2.8 $mg\ cm^{-2}$ Ni-FeTPP GDE were analyzed using scanning electron microscopy (SEM) (Fig.7).

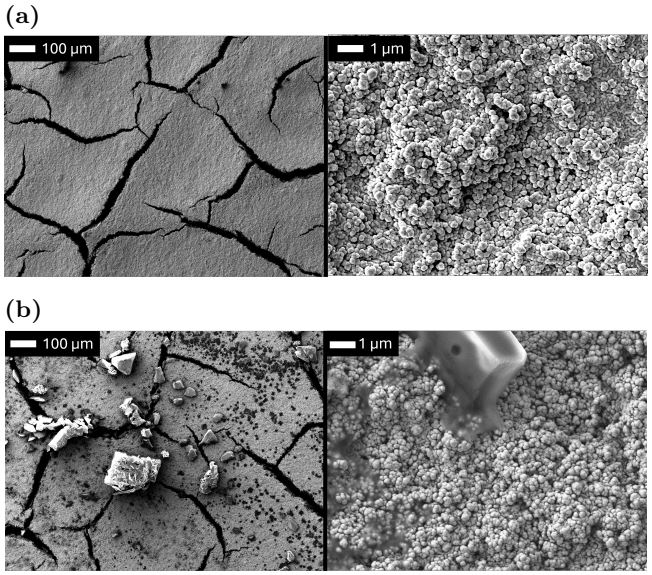

Figure 7: SEM surface morphology of **a)** Bare Ni-GDE. **b)** 2.8 $mg\ cm^{-2}$ FeTPP drop-casted on a Ni-GDE.

The comparison of the surface morphology between the two electrodes reveals the uneven distribution of FeTPP throughout the surface (Fig.7a & b). Relatively large FeTPP crystals can be seen unevenly spread throughout the Ni-GDE, providing a visual insight on the restricted Ni-FeTPP interaction by the drop-casting method. Therefore, drop-casting FeTPP on a Ni-GDE was deemed unsuitable to accomplish an even distribution across the GDE surface. Instead, we considered a better approach for coupling FeTPP to Ni, prior to deposition on the GDE.

3.1.2 Promoting a strong Ni-FeTPP electronic coupling by spray-deposition

A strong electronic coupling between nickel and FeTPP is required to ensure a non-redox mediated CO_2-to-ethanol reduction. This interaction confines FeTPP within the outer Helmholtz plane (OHP) during CO_2RR. Since drop-casting was unsuitable for achieving effective electronic interaction due to non-homogeneous distribution, we aimed to coat a mono-layer of FeTPP over nickel nanoparticles (Ni NPs) approximately 100 nm in size (Fig.8a) (for calculation see A.2). Following this idea, automated spray deposition was chosen for its effectiveness in improving material distribution on GDE surfaces compared to drop-casting.[35] To accomplish the deposition, we prepared a Ni-FeTPP catalyst ink and spray-deposited it onto a carbon-GDE, aiming to coat a mono-layer on every nickel nanoparticle, ensuring homogeneity.

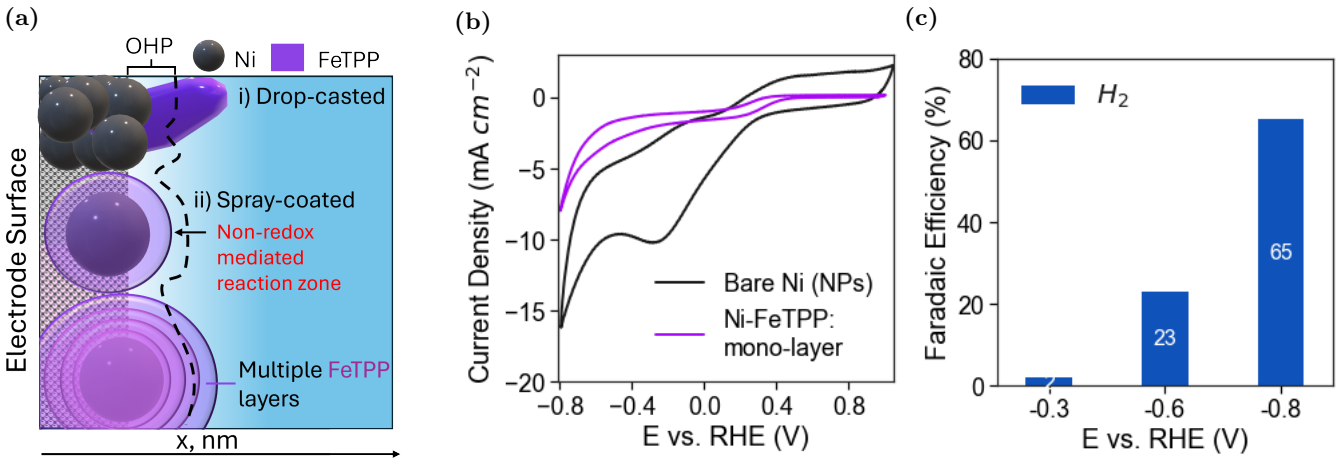

Figure 8: **a)**Drop-casting vs. spray-coating interaction schematics between Ni and FeTPP. By coating a mono-layer of FeTPP around a nickel nanoparticle, a strong electronic coupling is expected. This configuration aims to place FeTPP inside the electrical double layer (more specifically the outer Helmholtz plane or OHP), ensuring a non-redox electrochemical reaction by fixing the oxidation state of the metal center. In contrast, multiple layers would place FeTPP outside the electrical double layer, resulting in a redox-mediated CO_2RR. **b)** Cyclic voltammogram of Ni nanoparticles (Bare Ni NPs) and Ni-FeTPP mono-layer spray-coated on a C-GDE under CO_2 atmosphere. **c)** Faradaic efficiencies for the Ni-FeTPP mono-layer electrode calculated after 30 min of chronoamperometry at different reductive potentials under CO_2 (A.8).

The cyclic voltammogram (CV) of the FeTPP mono-layer (Fig.8b) exhibits a decreased current density compared to the bare Ni NPs. The higher current response of the bare Ni NPs is attributed to the reduction of NiO_x and α-$Ni(OH)_2$. Under ambient conditions, nickel forms a thin NiO layer, undergoing a $Ni^{2+/0}$ redox process during reductive polarization, as evidenced by the peak at -0.3 V_{RHE} (also discussed for sputtered Ni-GDE in A.2 and confirmed by x-ray diffraction characterization of the sputtered Ni-GDE A.10).[36]

Such difference in the CV curves between the Ni-FeTPP mono-layer and bare Ni NPs suggest they have interacted. For the Ni-FeTPP mono-layer, a relatively small peak at 0.3 V_{RHE} is seen, assigned to the $Fe^{3+/2+}$ couple of the FeTPP complex, as explained for Fig.5c. This behavior is similar to FeTPP drop-casted on a carbon GDE (A.5). We conducted an X-ray photo-electron spectroscopy (XPS) survey to confirm the presence of iron on the Ni-FeTPP mono-layer electrode, revealing a content of 0.16 atomic% on the surface (B.2).

However, no CO_2RR activity was detected after 30 minutes of electrolysis under different reductive potentials (Fig.8c). It is possible that the CO_2-to-CO conversion was inhibited by the intended strong Ni-FeTPP coupling, preventing *CO to release from the catalytic surface. If this were the case, ethanol or other C_{2+} products would have been detected, but no CO_2RR species were recorded. Therefore, an **unidentified phenomenon** is possibly inhibiting the intended Ni-FeTPP behavior.

To ensure the electrochemical activity of FeTPP for CO_2-to-CO reduction using the spray-deposition method, a higher loading of FeTPP was spray-coated along with Ni NPs, intending to form multiple

FeTPP "layers." A higher FeTPP loading could lead to its accumulation around a Ni nanoparticle; and due to FeTPP's poor conductive behavior several "layers" could potentially surpass the electrical double layer, as illustrated in Fig.8a.[34] This FeTPP positioning outside the outer Helmholtz plane (OHP) would facilitate *CO desorption through an $Fe^{2+/1+}$ redox process at reductive potentials more negative than -0.41 V_{RHE}.[30] Approximately 40 FeTPP "layers" were coated, chosen arbitrarily as a proof-of-concept.

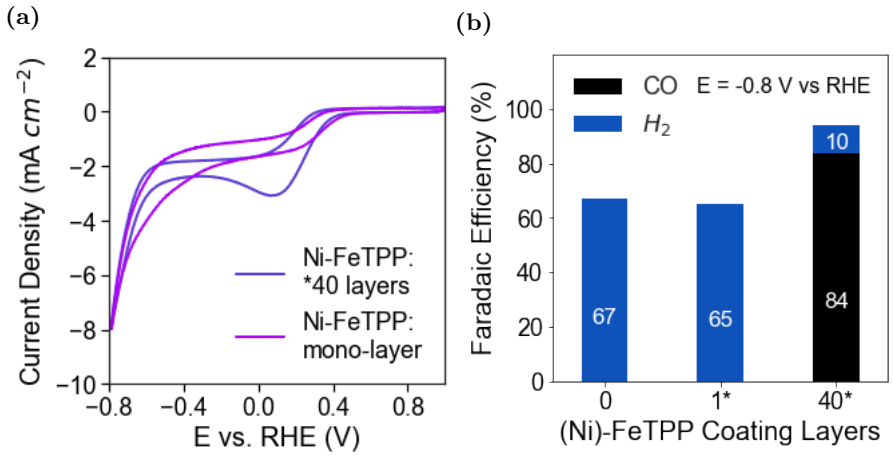

Figure 9: Electrochemical behaviour of 40 FeTPP layers on Ni NPs spray-coated on a C-GDE under CO_2 atmosphere. **a)** Cyclic voltammetry. **b)** Faradaic efficiencies reached after 30 min of chronoamperometry studies (A.8) under a reductive potential of -0.8 V_{RHE} for different FeTPP coating layers.
*The FeTPP coating layers were based on an assumed coating behavior. The 40 layers were upscaled based on the ink composition of the intended mono-layer (A.1). High-resolution transmission electron microscopy (TEM) could possibly confirm this assumption.

As expected, a higher iron redox activity is observed in the CV curve with 40 FeTPP layers compared to the mono-layer case (Fig.9). The redox peak at 0.3 V_{RHE} is attributed to the $Fe^{3+/2+}$ couple of the FeTPP complex. This increased current response is due to the higher FeTPP coating over the Ni NPs, which enhances the $Fe^{3+/2+}$ redox process.

More interestingly, the FEs at a reductive potential of -0.8 V_{RHE}, measured after 30 minutes of electrolysis, showcase a high CO_2-to-CO activity as expected from an FeTPP redox-mediated reaction. Notably, no ethanol was formed. This result is similar to the findings we obtained using the drop-casting technique (Fig.6c), which raises the new central question of our case study: **what electrode active-site interaction inhibits the CO_2-to-ethanol pathway electro-catalyzed by Ni-FeTPP?**

3.1.3 The electrochemical behavior of nickel

Understanding the electrochemical behavior of Ni is important to find a possible explanation to this puzzle. Abdinejad *et al.* reported that their Ni 3D electrode catalyzed CO_2-to-CO with a $FE_{CO} \approx 15\%$ at -0.4 V_{RHE}; a result not observed with our Ni GDEs.[29] This discrepancy under similar CO_2RR conditions (same potential range under 0.5 M $KHCO_3$) highlights the need to understand nickel's surface state. Hori *et al.* found that nickel showed poor activity in producing CO_2RR products even at potentials more negative than -0.8 V_{RHE} (pH 6.8), with FE_{H_2} exceeding 88.9%, and no CO detected. Instead, CH_4, C_2H_6, C_2H_2, and $HCOO^-$ were produced at potentials close to -1 V_{RHE}.[37] Nickel's poor CO_2RR activity is attributed to the high binding strength of *CO on its surface which prevents CO desorption.[38–41]

Hence, the surface state of Ni under reductive potentials requires further analysis to investigate a possible restriction of Ni-FeTPP strong electronic coupling, inhibiting our intended CO_2-to-ethanol pathway. A hint that might give way to the solution of this puzzle is the role of hydride species in Ni electrocatalysts. Nickel has been reported to form hydride species as a consequence of its catalytic activity for hydrogen evolution reaction (HER), which is intrinsically present during CO_2RR on aqueous media. Padavala and co-workers explained the formation of hydride species under mild temperature and pressure conditions during an electrochemical reaction by relating the electrochemical potential to H_2 fugacity through the Nernst equation.[42] The authors state that in metallic catalysts in protic solvents, protons react with electrons to form H_{ads} which drives the formation of hydride species (A6). It is proposed that under reductive potentials, H_{ads} diffuses into the metal lattice as H_{abs}, leading to the formation of α and β-hydrides. The β-MH_x phase represents a higher concentration of H_{abs}, resulting in structural reconfiguration and changes in electronic density.

The presence of nickel hydrides (NiH_x) can significantly influence reactivity by altering the electronic structure around them, as demonstrated by Hall *et al.* In their study, the researchers investigated the activity of a solid Ni electrode in an alkaline medium. They proposed that inhibition during hydrogen evolution reaction (HER) is caused by a structural change in metallic Ni under cathodic polarization due to H_{abs} atoms rapidly diffusing into the metal lattice structure. Consequently, H_{abs} content starts to build up near the grain edges until it reaches a critical value. When this condition is met, metallic Ni transforms into α-NiH_x and β-NiH_x, reducing its HER activity. This transformation is reported to alter the electronic structure across the entire Ni surface. An earlier study by Soares *et al.* also demonstrated this behavior, where the formation of bulk β-NiH_x was observed.[43]

Consequently, it is logical to question the influence of NiH_x on the intended strong electronic coupling between Ni and FeTPP, which could inhibit the CO_2-to-ethanol pathway. In the context of CO_2RR, Pd—a metallic catalyst similar to Ni—is known to form hydride phases and function as both HER and CO_2RR electrocatalyst, and has been extensively studied.[44,45] These studies evaluated the effect of Pd hydride species in CO_2RR and reported a decrease in the binding strength of *CO and other reaction intermediates such as *HCOO and *COOH. These findings suggest a potential inhibiting effect of NiH_x species on our system, possibly affecting the intended strong electrode active-sites interaction when coupling Ni with FeTPP for CO_2-to-ethanol reduction.

Research around this topic is limited and challenging, as the lattice expansion caused by NiH_x formation reverses when the electrochemical potential is removed.[42] However, based on the clues gathered throughout this study and considering the potential direct effect of the surface state of nickel on our Ni-FeTPP interaction, we can speculate that the formation of NiH_x species can play a role in altering the electronic structure of Ni electrodes during CO_2RR.

3.1.4 Time scales and geometric effects: a clue into the unknown surface state of nickel

In the study by Abdinejad *et al.* a relatively large, porous 16x32x5 mm Ni 3D electrode with internal hollow square ducts was used.[29] The authors analyzed the surface morphology of their 3D electrode using SEM, revealing large ($\approx 5\ \mu m$), non-symmetrical Ni particle structures (Fig.10a). Considering

the potential NiHx layer formation, the large particle dimensions of the electrode would promote slow diffusion of H_{abs}, rapidly forming an α-NiH_x phase at the surface that quickly transitions to the β-phase. This rapid transition is due to the increased concentration of H_{abs} at the surface, caused by the delayed diffusion of H_{abs} resulting from geometric effects.

How is this diffusion effect different in our Ni GDEs?
The H_{abs} diffusion our Ni GDEs experience is different due to the smaller Ni particle sizes ($\approx$50 nm for the spray-coated and $\approx$100 nm for the sputtered GDEs) and the more abundant grain edges clearly observed for our sputtered and spray-coated Ni-GDEs (Fig.7, A.12). This structural difference allows for more rapid diffusion of H_{abs}, likely delaying the formation of a β-NiH_x layer.[46] The absence of this β-NiH_x layer could alter the electronic structure of our Ni electrodes and their interaction with the FeTPP active-site within the electrochemical double layer, compared to the larger particle-size structure of the Ni 3D electrode. This difference might inhibit the intended CO_2-to-ethanol pathway in our Ni-FeTPP GDEs.

To gain additional insight into the magnitude of this possible geometric effect, we modeled the characteristic time for diffusion (t_d) by solving Fick's second law for a simplified 1D case. According to Deen (2012), t_d provides an estimate of how long it takes to observe a concentration change at a given distance.[47] In our context, it indicates the time required for H_{abs} to diffuse through a Ni spherical particle. We hypothesize that the longer it takes for hydrogen to diffuse through a Ni particle, the more likely it is for the particle to build up H_{abs} concentration close to the surface, potentially leading to the formation of β-NiH_x species under reductive polarization.

This approach considers the diffusion coefficient of hydrogen on metallic nickel and the characteristic length of a particle size, assuming that the system is not affected by the electric field, electrolyte interactions, or the partial pressures of other species. This method can provide additional understanding of the time scales that the two systems may be subject to in terms of NiH_x formation. For the model, we considered two characteristic particle sizes (δ): 5 μm and 100 nm, representing the particle diameters of the Ni 3D electrode and our Ni GDEs, respectively.

$$\frac{dC}{dt} = D\frac{d^2C}{dx^2} \tag{1}$$

By implementing characteristic scales to Eqn.1 and applying $O(1)$ scaling to the time-dependent term and the diffusion term, and then rearranging the resulting equation (see B.3), t_d can be calculated:

$$\boxed{t_d = \frac{\delta^2}{D}} \tag{2}$$

$$\boxed{t_{d-5\mu m} = 446\ s} \text{ vs. } \boxed{t_{d-100nm} = 0.18\ s}$$

The 3-order magnitude difference in the t_d for the different electrode particle sizes (Fig.10a) offers additional insight into the diffusion effects experienced by the two electrodes. Although this understanding is limited by the assumptions of a 1D model that considers only diffusion effects, it can guide the research towards the possibility of unintended interactions promoted by geometric effects. To visualize the diffusion evolution in the different Ni particle sizes, the analytical solution of Eqn.1 was modeled for the two electrodes, based on the assumptions of a semi-infinite diffusion model with a fixed mormalized boundary concentration of H_{abs} (see B.3).

Our model (Fig.10c & d) shows the rapid diffusion of H_{abs} experienced by the Ni GDE particles compared to the 3D electrode. The slower diffusion in the 3D electrode particles results in a higher H_{abs} concentration near the particle surface, potentially leading to the formation of β-NiHx. Since the surface depth affecting the strong electronic coupling between Ni and FeTPP is likely within 1 nm of the Ni surface, the model shows that the impact of H_{abs} rapidly decreases for the Ni GDE compared to the 3D electrode, which experiences a sustained H surface concentration (Fig.10d). We hypothesize

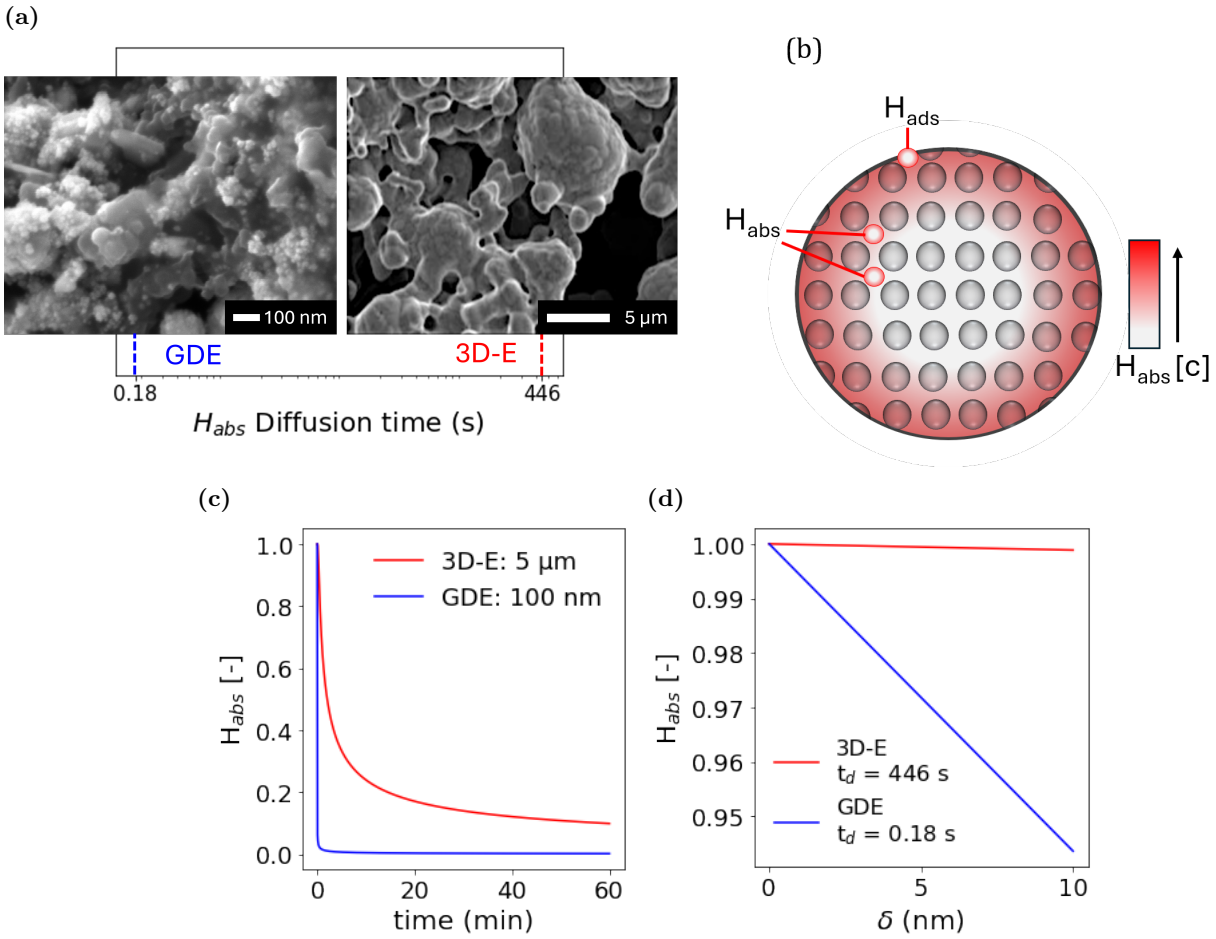

Figure 10: **a)** SEM images of the size of Ni-NPs of the spray-coated GDE compared to the 3D electrode (3D-E), locating them on their characteristic H_{abs}-t_d calculated by Eqn.9.[29] **b)** Proposed diffusion profile schematic inside a relatively big nickel particle. The concentration of H_{abs} builds up close to the surface of the particle as t_d increases for bigger particle sizes. **c)** 1D model of the normalized H_{abs} concentration profile as a function of time, and **d)** as a function of the diffusion length for the different Ni electrode's characteristic (t_d) in a penetration depth of 10 nanometers.

that the more abundant grain boundaries in our Ni GDEs enhance the H_{abs} diffusion, keeping the NiH_x content below the critical value to form β-NiH_x.

Additional experimental data is needed to improve the simulation by incorporating kinetic constants for NiH_x species formation under the influence of reductive currents and the presence of surrounding species during CO_2RR. This model may provide insights into the different NiH_x phases that bulk particle sizes are subjected to. However, the effect of this interaction on the strong electronic coupling between Ni and FeTPP during CO_2RR still needs to be evaluated to solve the puzzle. Specifically, it remains to be explained why our system could catalyze CO_2-to-CO through a redox-mediated process by Ni-FeTPP but fails to reduce CO_2-to-ethanol when the redox-mediated process is intended to be eliminated. All the evidence gathered throughout this project, gives way to highlight the challenging translation of a hybrid molecular catalyst into a GDE, which requires a profound understanding of all the phenomena involved. Nevertheless, we believe this work may pave the way for further research to solve the puzzle, aiming for the intended selective CO_2-to-ethanol reduction by Ni-FeTPP.

3.1.5 Future outlook: where should research efforts concentrate?

To further confirm our hypothesis that explains the inhibitory effect our Ni-FeTPP GDEs may experience during CO_2RR that restricts the CO_2-to-ethanol pathway, we propose the following measurements:

1. **Confirm the surface state of Ni during CO_2RR conditions**: Performing operando measurements is highly recommended. X-ray diffraction (XRD) with a high x-ray flux provided by a Synchrotron facility would give us an insight on the structural changes by a possible NiH_x formation. This could give us an approximate H content in the lattice structure to see the dominant NiH_x species in our GDE's under CO_2RR conditions.[42,48]

2. **Confirm the strong electronic coupling of Ni and FeTPP during CO_2RR** To determine the fixed oxidation state of iron during operation, X-ray absorption spectroscopy (XAS) techniques can be employed.[49] X-ray absorption near-edge structure (XANES) can determine the oxidation state of iron during CO_2RR, as well as provide information about the coordination environment. Extended X-ray absorption fine structure (EXAFS) can reveal the local environment of the absorbing atom, including bond distances and coordination numbers. This information can help determine whether the intended strong electronic coupling between Ni and FeTPP maintains the reaction as non-redox-mediated, and confirms if this interaction is affected by potential NiH_x species formation.

Finally, complementing the in situ/operando experimental observations with DFT calculations could illuminate the unidentified phenomena observed in our Ni-FeTPP hybrid electrodes. However, it is crucial to note that these techniques require careful consideration due to their limited availability and cost. We believe this direction merits further research focus. This case study addressed our research question by underscoring the significance of understanding how subtle changes in the microenvironment can profoundly impact electrode active-site interactions. It also highlighted the challenges associated with translating a hybrid molecular system to a GDE-based system to enhance the selectivity of CO_2RR beyond CO. I believe this research will contribute to a deeper understanding of hybrid molecular systems, paving the way for future scalability.

3.2 Local environment interaction *proof-of-concept*: CoPc for CO_2-to-methanol

As the electrode active-site interaction case study limited our ability to modify the micro-environment to enhance C_{2+} product selectivity; we focused on a hybrid molecular catalyst system that has been reported to reduce CO_2-to-methanol effectively on a GDE-based electrolyzer. Research around Cobalt Phthalocyanyne (CoPc) has been centered towards understanding the local environment interactions by changing the type of support and integrating the role of the binding energies between the active sites and CO_2/CO.

For a hybrid CoPc system, multi walled carbon nanotubes (MWCNT) have proven to be an effective support. They homogeneously distribute the complex and prevent cobalt-cobalt interactions that might compromise the single-atom active sites needed for CO_2 or CO binding.[50] This setup has ensured a high dispersion, reducing catalyst aggregation. McCrory and co-workers[51] evaluated the binding strengths between the CoPc/MWCNT active sites with CO_2 and CO to further understand the CO_2-to-methanol pathway by this hybrid molecular complex. They found that CO_2 has a 3 times higher binding strength than CO to CoPc (Fig.11a). This causes *CO displacement by a CO_2 molecule before it can be further reduced. Therefore, to achieve CO_2-to-methanol conversion, the partial pressure of CO (P_{CO}) must be sufficiently high relative to the partial pressure of CO_2 (P_{CO_2}).

The starting point of our case study was evaluating the CoPc/MWCNT system, focusing on the competing behavior between CO_2 and CO for electrochemical active sites. We aimed to enhance CO_2-to-methanol selectivity by engineering the catalyst layer (CL) of the GDE to increase the local CO concentration. We chose a super hydrophobic expanded polytetrafluoroethylene (ePTFE) electrode because it has proven to resist flooding and achieve higher C_{2+} selectivities compared to carbon-based GDEs (C-GDEs).[52] Due to their non-conductive nature, ePTFE electrodes were sputtered with a 100 nm Ag layer (Ag-ePTFE) to serve as a current collector and potentially act as a CO_2-to-CO tandem source. To achieve a homogeneous catalyst dispersion, a CoPc/MWCNT (referred to as CoPc) suspension was spray-deposited onto Ag-ePTFE electrodes (Fig.11d). A threshold CO_2 conversion value $X_{CO_2} = 30\%$ was determined as a requirement for the CO_2-to-methanol pathway.[51] To achieve this, we used N_2 to dilute the CO_2 delivered to the catalyst layer micro-environment due to its inert behavior under CO_2RR conditions. This setup aimed to achieve a high P_{CO} relative to PCO_2 by mixing the CO_2 source with N_2 (Fig.11c).

While the system has many variables, the CO_2/N_2 ratio, flow rate, and current density were kept constant to focus on engineering the CL rather than optimizing parameters (Fig.11b). The current density value was determined based on the theoretical conversion of 5sccm of CO_2 (see C.1). Our objective was to conduct a proof-of-concept study to enhance Co_2-to-methanol selectivity by modifying the micro-environment of the catalyst layer of a GDE; using the Faradaic efficiency of methanol (FE_{CH_3OH}) as the performance metric.

We evaluated the electrochemical behavior of our base-case CoPc system under CO_2 and CO to determine the maximum FE_{CH_3OH} that our base-case can reach for CO_2RR and CORR, repectively (Fig.12).

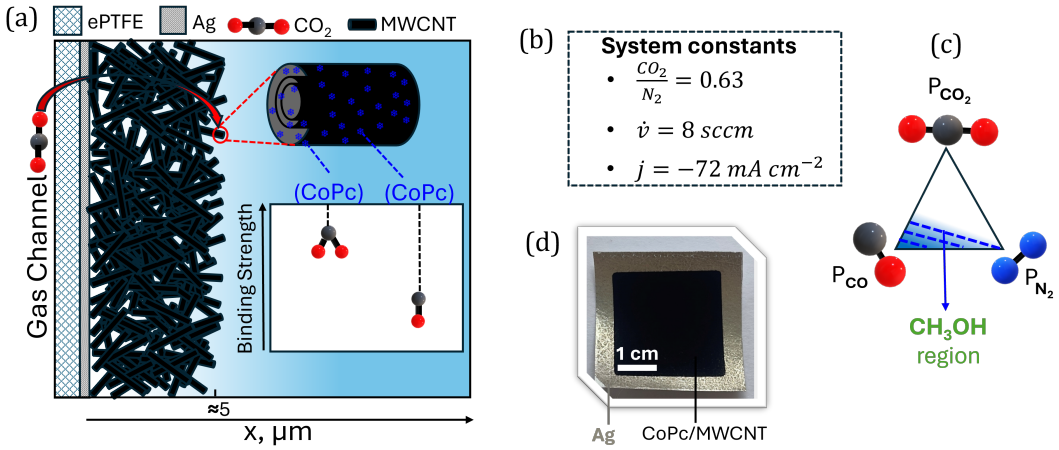

Figure 11: **a)** Catalyst layer configuration. As CO_2 in solution reaches a CoPc/MWCNT active site, it's more likely to undergo reduction than CO due to it's higher binding strength. **b)** System constants throughout the case study unless otherwise stated: CO_2/N_2 ratio, gas volumetric flowrate and current density during chronopotentiometry studies. **c)** Intended partial pressures equilibrium diagram between CO_2, N_2 and CO. For the system to be able to reduce CO_2-to-methanol, the partial pressure of CO needs to be high enough to compete against the more favourable binding between CO_2 and CoPc. **d)** Spray-coated CoPc (3wt%)/MWCNT with a total loading of 0.5 $mg\ cm^{-2}$ ($5cm^2$ total covered area) over 100 nm Ag sputtered ePTFE.

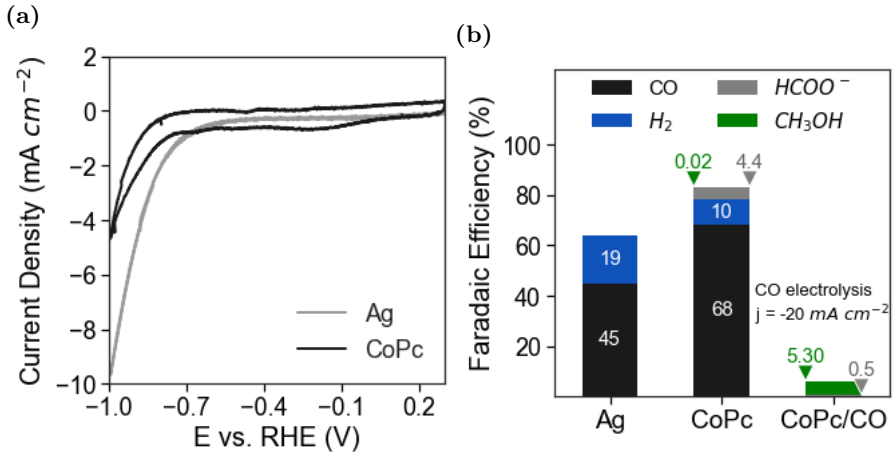

Figure 12: Behaviour of bare Ag (100 nm) sputtered on ePTFE under CO_2 atmosphere and CoPc 3 wt% spraycoated on Ag-ePTFE **a)** Bare Ag cyclic voltamogram **b)** Faradaic efficiency after 30 min of chronopotentiometry at a fixed current **c)** CoPc Cyclic voltammetry **d)** Faradaic efficiency of liquid products after 30 min of chronopotentiometry studies under a reductive current of -20 $mA\ cm^{-2}$ (A.17).

We observe higher Ag activity during cyclic voltammetry compared to our CoPc base-case (Fig.12a). This increased current density is partly due to a higher HER rate. As expected, the CoPc base-case achieves higher CO_2RR products than the thin 100 nm Ag catalyst layer (CL). According to van Montfort and co-workers, thin 50-100 nm CLs on ePTFE electrodes exhibit low activities due to poor in-plane current distribution across the catalyst surface.[52] This results in electrochemical activity being concentrated at the borders of the current collector, thereby limiting the number of electrochemically active sites. To address this, a thicker catalyst layer (CL) with an added molecular catalyst supported on a conductive substrate such as MWCNT, with an optimal thickness between 1-5 μm, is used. Hence our CoPc system achieves higher Co_2RR activity by providing a greater number of electrochemically active sites.[53] The system's inability to reach 100% total Faradaic efficiency (FE) is attributed to the underestimation of our total gas outflow influenced by the dilution in N_2. However, we deemed this factor not pivotal in our case study as we mainly focused on the liquid products.

From the CORR tests, we determined that our base-case can only achieve a $FE_{CH_3OH} = 5.3\%$ with a $j_{CH_3OH} = -0.95 mA cm^{-2}$. This performance is significantly lower compared to the CORR results reported by Ren and co-workers, whose system achieved a $FE_{CH_3OH} = 65\%$ with a $j_{CH_3OH} = -19.5\ mA\ cm^{-2}$.[50] However, we used our base-case as a starting point to demonstrate the potential for further enhancement of the CO_2-to-methanol selectivity through micro-environment engineering rather than by optimizing the parameters.

3.2.1 Engineering the CoPc/MWCNT micro-environment

The following modifications were done to our CoPc base-case to promote a higher CO_2-to-methanol selectivity (Fig.12a):

1. **Direct promotion of CO availability**: The incorporation of silver NPs was considered due to silver's well known catalytic activity for CO_2-to-CO. Ag NPs systems in specific have reported $FE_{CO} = 92\%$ when deposited on C-GDEs.[54] Thus, incorporating an additional 20 wt% ratio of the catalyst with respect to our CoPc/MWCNT base-case was expected to enhance the local CO concentration. This would create additional electrochemical active sites to promote CO_2-to-CO conversion, ensuring CO availability near the CoPc active sites to facilitate CO_2-to-methanol reduction.

2. **Creation of hydrophobic gas channels**: The incorporation of PTFE particles in the catalyst layer (CL) creates a hydrophobic environment, which has proven to enhance CO_2 mass transport during CO_2RR. In a study conducted by Xing and co-workers using cupper nanoparticles, it was demonstrated that introducing PTFE particles into the CL benefits CO_2RR.[55] The authors attribute this advantage to the reduction of CO_2 diffusion length (δ) through the GDE's catalyst layer. This reduction is achieved by creating hydrophobic gas channels that facilitate gas-phase transport. This allows faster CO_2 diffusion through the catalyst layer directly to the surface-electrolyte boundary for its further reduction. Additionally, the hydrophobic gas channels increase the CO concentration near the CoPc active sites by creating gas 'traps', thereby enabling our intended CO_2-to-methanol pathway. To achieve this, an additional 50 wt% ratio with respect to CoPc/MWCNT was incorporated into our base-case GDE. However, such a change in hydrophobicity, while enhancing CO availability, could compromise the contact area between the electrolyte and active sites. This compromise might limit the number of reaction sites; but our initial results show promise (Fig.13b & c).

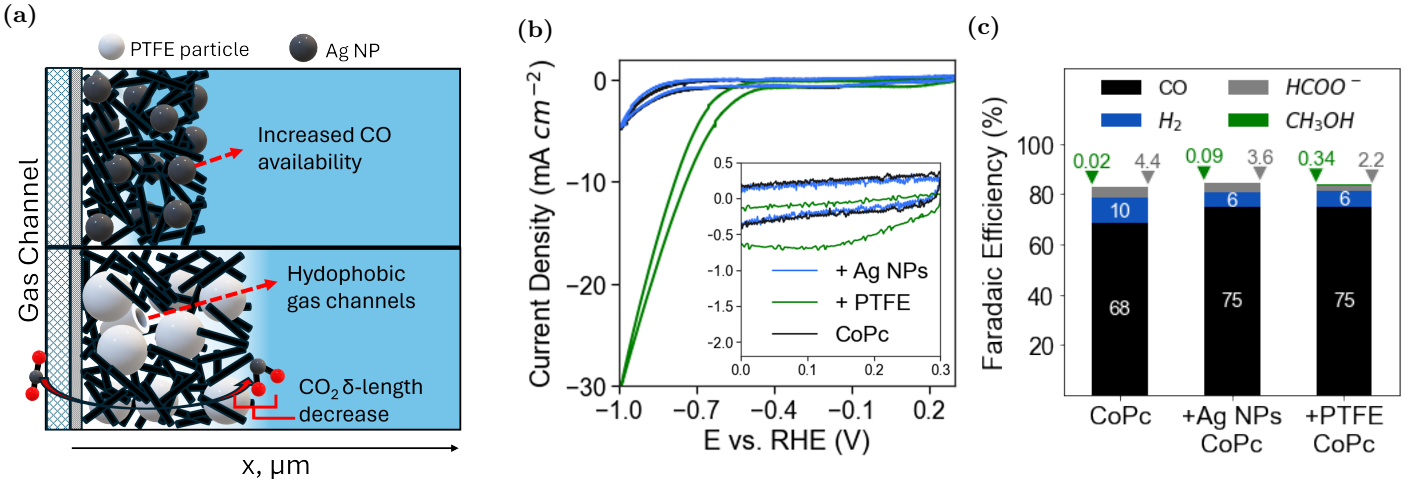

Figure 13: **a)** Micro-environment changes to the CoPc/MWCNT base case on the GDE's catalyst layer. Top: incorporation of Ag NPs. Bottom: incorporation of PTFE particles. Behaviour of the modified CoPc electrodes on incorated PTFE particles (+PTFE) and incorporated Ag NPs (+Ag NPs) under CO_2/N_2 atmosphere. **b)** Cyclic Voltammetry, and inset view at a potential range between 0 - 0.3 V_{RHE}. **c)** Faradaic Efficiencies calculated after 30 min of chronopotentiometry at a reductive current of -72 $mA\ cm^{-2}$ (A.19).

In Fig.13b, we can see a clear distinction: the electrode with incorporated PTFE exhibits a higher current density response during CV compared to the base case. This observation aligns with our expectations that modifying the micro-environment to enhance CO_2 mass transport would increase the local CO concentration and promote C-C coupling.[56] This enhancement is evident with the FE_{CH_3OH} of our base case being increased by a remarkable 17-fold (Fig.13c). Similarly, our modified base-case with incorporated silver nanoparticles achieved a four-fold increase in the FE_{CH_3OH}, confirming our expectation that methanol selectivity can be enhanced for the CoPc/MWCNT case by increasing the local CO concentration.

Interestingly, our results reveal an intriguing phenomenon: a increase in current response within a potential range known for non-faradaic processes (inset in Fig.13b). This current response at this specific potential region likely reflects the double layer capacitance, which is directly proportional to the electrochemical surface area (ECSA).[57] Surprisingly, the CoPc + PTFE electrode displays a higher capacitive current response than our CoPc base-case and the +Ag NPs GDEs. This contradicts our initial expectations, as an increase in hydrophobicity would intuitively suggest reduced contact area between the active sites and the electrolyte. Thus, the addition of Ag NPs should theoretically create more electrochemical active sites, implying a greater ECSA than our CoPc base-case and CoPc + PTFE GDEs. To understand this behavior, we characterized the modified electrodes and compared them to the base-case by analyzing their surface morphology using scanning electron microscopy (SEM) (Fig.14).

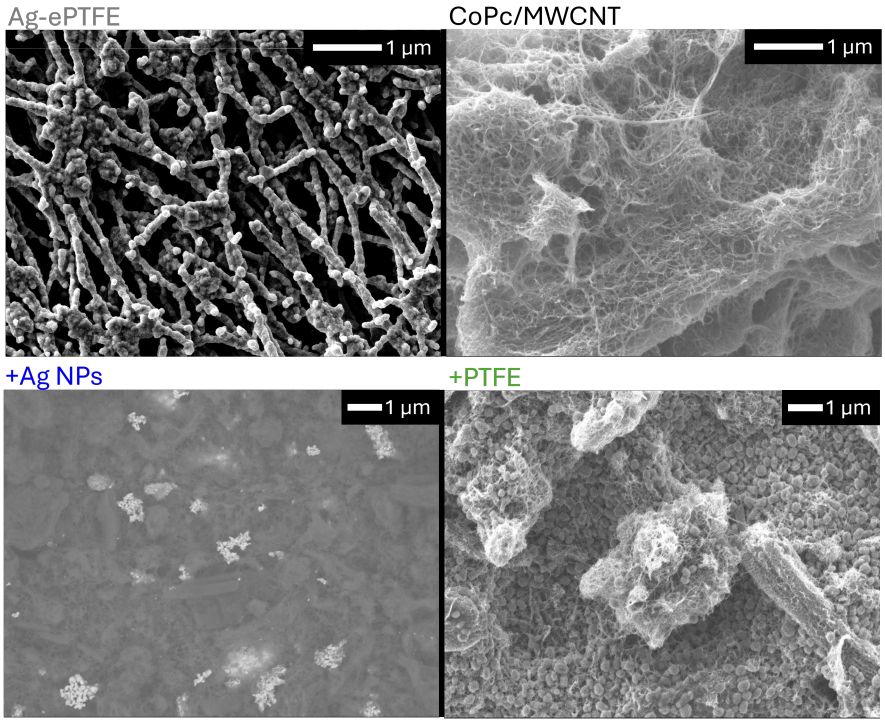

Figure 14: SEM images of the different catalyst layers from the GDEs tested in this case study were taken at a resolution of 1 μm. The Ag-ePTFE shows a clear adhesion onto the ePTFE fibers by the sputtering deposition method. The base-case CoPc/MWCNT shows a web-like, well-spread distribution of MWCNTs, anchored together by Nafion binder (A.22).

The surface morphology of the CoPc + Ag NPs case reveals Ag NPs agglomeration. This agglomeration explains why the current response from the +Ag NPs is similar to the CoPc base-case and lower than that of the +PTFE case, as catalyst agglomeration reduces the total electrochemical surface area (ECSA) by decreasing the number of active sites[58]. However, this information suggests the potential for further enhancing the four-fold increase in performance by ensuring a homogeneous distribution during deposition on the gas diffusion electrode (GDE).

In the CoPc + PTFE case, the SEM image shows a homogeneous distribution of PTFE particles within the catalyst layer, confirming the presence of hydrophobic gas channels. These channels reduce CO_2 diffusion length, thereby facilitating the delivery of CO_2 to the electrolyte interface. This characterization reflects the results obtained in Fig.13, as the modification of the micro-environment in the CoPc + PTFE case enhances the selectivity towards methanol when compared to our base-case.

Both of our engineered CoPc/MWCNT GDEs demonstrate promising results in their electrochemical performance during CO_2RR. When compared to our base-case, the CoPc + Ag NPs GDE exhibited a four-fold increase in methanol selectivity, while the CoPc + PTFE case shows a remarkable 17-fold increase. These findings address our research question by showcasing enhanced methanol selectivity through the engineering of the micro-environment of the catalyst layer for a hybrid molecular catalyst system. Our results pave the way for further advancements in molecular catalyst-hybrid systems design by introducing micro-environment changes that have proven to enhance methanol selectivity.

3.2.2 Future Outlook

Our successful proof-of-concept study on enhancing selectivity through changes in the micro-environment of the catalyst layer opens the possibility to further improve any hybrid molecular system. Hence, the following proposals to address the follow-up research are presented:

1. **Catalyst/support dispersion method**: We emphasize the importance of the dispersion method used when anchoring the molecular catalyst onto the support. McCrory and colleagues have established a meticulous procedure for the dispersion of CoPc on MWCNT, which, if followed, could lead to the optimization of the CoPc/MWCNT hybrid system.[51]

2. **Ion exchange membrane**: Another factor that merits further attention is the selection of the ion exchange membrane. The phenomenon of electro-osmotic drag, associated with the movement of ions under an electric field, results in the formation of an electrical double layer between the membrane and electrolyte interface.[59] Depending on the type of membrane, charges can migrate through it, potentially allowing C_{2+} products to crossover towards the anolyte.[60] Therefore, it is crucial to choose ion exchange membranes that effectively prevent product crossover, such as the Nafion 117 cation exchange membrane.[54]

3. **Temperature and cation effect**: Evaluating the effect of temperature on the selectivity of C_{2+} products by hybrid molecular catalysts could serve as an intriguing follow-up to this research. With research infrastructure on higher-temperature CO_2RR expanding but still limited, exploring temperature variations could provide valuable insights in the context of hybrid molecular systems. Additionally, the cation effect has been shown to enhance product selectivity, suggesting that testing different electrolytes could significantly impact the catalytic performance of hybrid molecular catalyst systems in enhancing C_{2+} product selectivity.[61]

This case study successfully demonstrated the enhancement of methanol selectivity by engineering the micro-environment of a hybrid molecular catalytic system, establishing a base-case that paves the way for further research and optimization.

4 Conclusion

The impact of subtle changes to the micro-environment belonging to hybrid molecular catalysts was explored in this study, with the aim of optimizing electrochemical reduction of CO_2 beyond CO. To reiterate, we examined the challenges of translating the electrode active-site interaction of a Ni-FeTPP system, from a 3D electrode to a GDE-based electrolyzer. Drop-casting and spray deposition methods were used to promote strong electronic coupling between nickel and FeTPP, which would ultimately enable the non-redox mediated CO2-to-ethanol pathway. Our electrocatalysts however, did not achieve ethanol production. A likely explanation for this ethanol production inhibition is the possible effect of NiH_x species formation during CO_2RR, which could alter the Ni-FeTPP electronic interaction during CO_2RR. Understanding these effects could help refine Ni-based systems and pave the way for effective CO_2-to-ethanol reduction electro-catalyzed by Ni-FeTPP.

Furthermore, micro-engineering the local environment by promoting a higher local CO concentration resulted in an increased CO_2-to-methanol selectivity in a CoPc/MWCNT setup. We achieved a remarkable 4-fold increase in methanol Faradaic efficiency by incorporating silver nanoparticles that provide additional CO close to the CoPc active sites. Even better results were obtained with an outstanding 17-fold increase in methanol selectivity by incorporating PTFE particles. This demonstrated that creating hydrophobic gas channels enhances CO_2 mass transport by decreasing the diffusion length of CO_2 to the reaction site, creating gas traps that increase the local CO concentration for further reduction. These results lay the groundwork for further advancements in molecular catalyst-hybrid systems, by introducing micro-environment changes that have proven to enhance selectivity beyond CO, which can be applied to other GDE-based configurations.

By combining the knowledge gathered in this study, we have proved that subtle changes in the micro-environment can significantly impact CO_2 reduction beyond CO. This underscores the importance of continuing to research alternative electrocatalysts that can efficiently store renewable electrons as fuels and feed-stock chemicals; a crucial step as our world transitions towards alternative energy sources in the coming decades.

A Appendix

A Experimental

A.1 Initial Areal Loading of FeTPP on Ni-GDEs

- Mass of Ni 3D electrode = 3.451 g Ni
- Drop-casted FeTPP mass onto Ni 3D electrode = 130 mg FeTPP
- Ratio FeTPP/Ni wt% = 3.767%, considered as 3wt% for the translation
- **Mass of 300 nm ($3x10^{-5}cm$) Ni layer for our Ni-GDEs:**
- Area of Ni-GDEs = 4 cm^2
- Volume of Ni in Ni-GDEs, V_{Ni}= 4 cm^2 $3x10^{-5}cm = 1.2x10^{-4}cm^3$
- Mass of Ni = V_{Ni} x $\rho_{Ni} = 1.2x10^{-4}cm^3$ x 8.9 g $cm^{-3} = 1.068x^{-3}g = 1.068mgNi$
- Mass of FeTPP required = 1068 mg Ni x $\frac{3wt\%}{100\%} = 0.032$ mg FeTPP
- Final areal loading = $\frac{0.032\ mg\ FeTPP}{2.25\ cm^2} = 0.0142\ mg\ cm^{-2}$

A.2 FeTPP mono-layer over Ni nanoparticles calculation

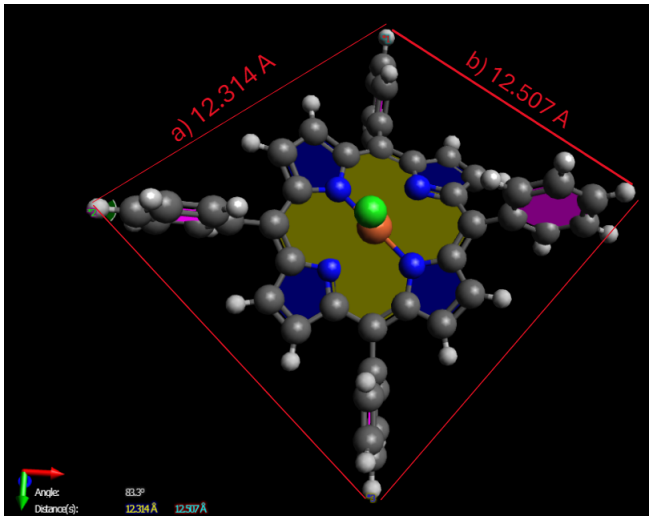

Figure A.1: FeTPP molecule simulated in Avogadro

The surface area of one FeTPP molecule was modeled using Avogadro Software (A.1) resulting in a total area of 1.54 $nm^1/molecule$. The surface area of a 100 nm nanoparticle at a distance of 2 Å was calculated as:

- $SA = 4\pi r^2 = 4\pi(50nm)^2 = 3415.93\ nm^2$
- To calculate the number of FeTPP molecules required to cover all the surface are of 1 Ni nanosphere: $\frac{3415.93\ nm^2}{1.54\ nm^2/FeTPPmolecule}$= 20399.95 FeTPP molecules
- To determine the molar mass required to cover a Ni nanoparticle: $20399.95FeTPPmolecules\ x\ \frac{1molFeTPP}{N_A=6.022x10^{23}!molucules} = 3.39x10^{-20}$ mol FeTPP/Ni nanosphere.
- Finally, the mass of 1 Ni nanosphere to determine the FeTPP loading content was determined as: $M_{Ni} = \rho_{Ni}\ x\ V_{Ni,r=50nm} = 8.908\ g\ cm^{-3}\ x\ 5.236x10^{-16}\ cm^{-3} = 4.66x10^{-12}$ mg Ni/Ni nanosphere

- For the ink preparation, 2.5 mg of Ni were considered to spray-deposit onto the carbon GDE, giving a total FeTPP loading of 0.0128 mg FeTPP/2.5 mg Ni. The same procedure was up-scaled for the ≈ 40 layers case.

A.3 Faradaic Efficiency Calculation

For the estimation of the Faradaic efficiency of gaseous products, the fractions of H_2 and CO were determined by GC injections and used in the following formula:

$$n_{CO} = \dot{V}\text{outlet} \cdot X_{CO} \tag{3}$$

$$n_{H2} = \dot{V}\text{outlet} \cdot X_{\mathrm{H_2}} \tag{4}$$

$$FE_{CO} = \left(\frac{n_{CO}\ F\ n_e}{I}\right) \cdot 100\% \tag{5}$$

Where: n_{CO} = moles of CO produced, n_e- number of electrons involved, F = Faradays Constant = 96485 $C\ mol^{-1}$, and I = applied current (A).
The calculation of the Faradaic efficiency of liquid products followed the same procedure after integration of the H-NMR peaks, taking into account the volume used for the sample and the total volume of the recirculating catholyte.

B Electrode-active site interaction

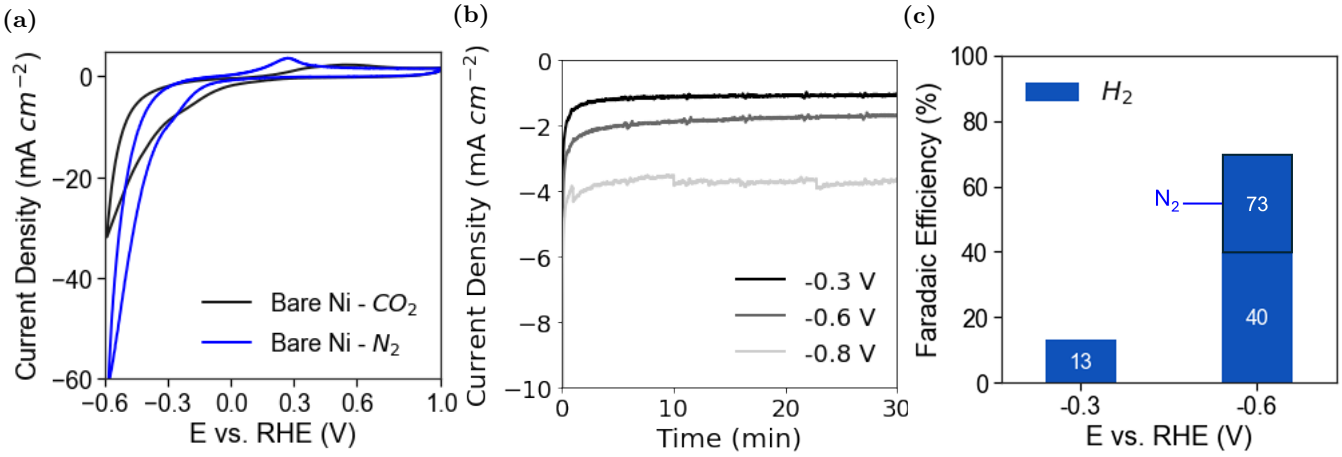

Figure A.2: Electrochemical activity of sputtered 300 nm Ni on C-GDE **a)** Cyclic voltammogram under CO_2 and N_2 atmospheres.**b)** Chronoamperometry at different reductive potentials under CO_2. **c)** Faradaic efficiencies after 30 min of electrolysis at different reductive potentials

The oxidation peak in the cyclic voltammogram (CV) (A.2a) found at 0.25 V_{RHE} under N_2 is attributed to the formation of NiO_x and α-$Ni(OH)_2$ also seen by Machado *et al.* in alkaline media.[62] This follows the reduction to metallic nickel ($Ni^{2+/0}$) at -0.3 V_{RHE}.

Shifting from a N_2 to CO_2 atmosphere decreases the current density as nickel is poisoned by produced CO.[63] This is seen on a passivating effect on the 0.25 V_{RHE} peak when comparing the CVs under N_2 and CO_2 (Fig.A.2a). This effect is also evident from the higher FE_{H_2} achieved under a N_2 atmosphere compared to CO_2 (FigA.2c). The system's inability to reach 100% FE is attributed to the low current densities (FigA.2b) , which amplify the impact of possible side reactions on the total FE. As the potential becomes more negative, a higher FE_{H_2} is reached as HER becomes more predominant.[31]

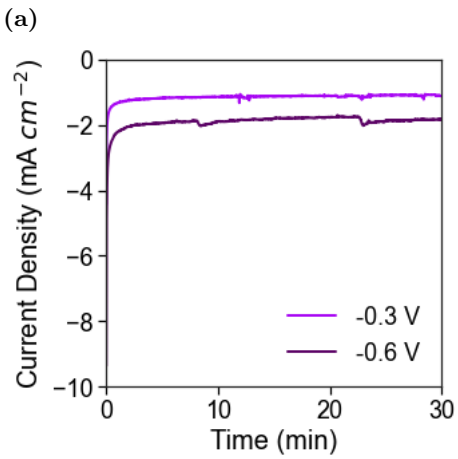

Figure A.3: Chronoamperometry at different reductive potentials under CO_2 atmosphere for FeTPP dropcasted on pre-sputtered Ni on C-GDE under CO_2 atmosphere. with an areal loading of a) 0.0142 $mg\ cm^{-2}$

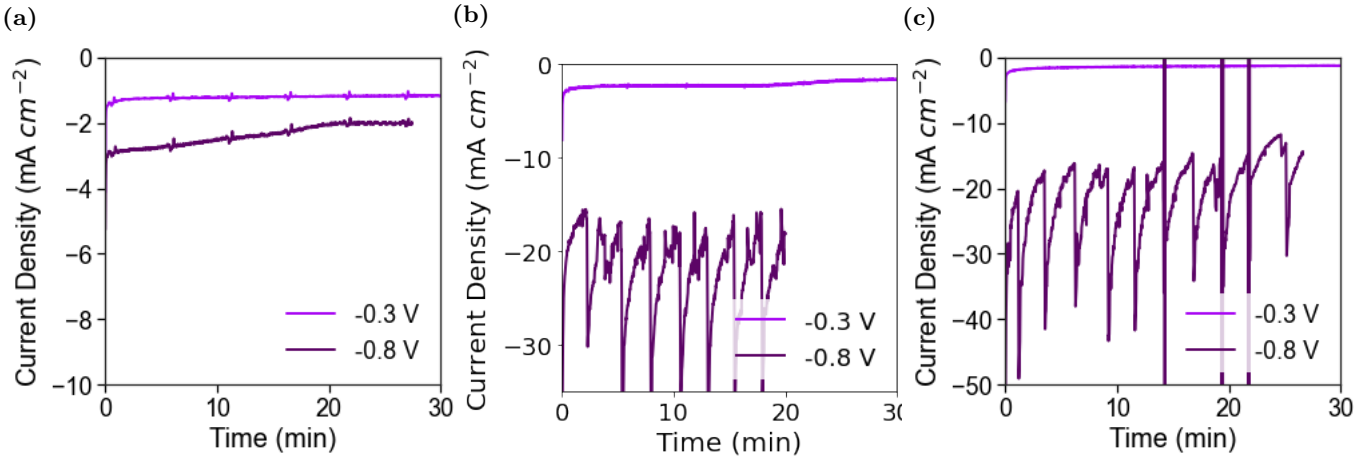

Figure A.4: Chronoamperometry at different reductive potentials (V_{RHE}) for FeTP drop-casted on Ni-GDEs at loadings of **a)** 1.4 $mg\ cm^{-2}$, **b)** 2.8 $mg\ cm^{-2}$, and **c)** 6.5 $mg\ cm^{-2}$

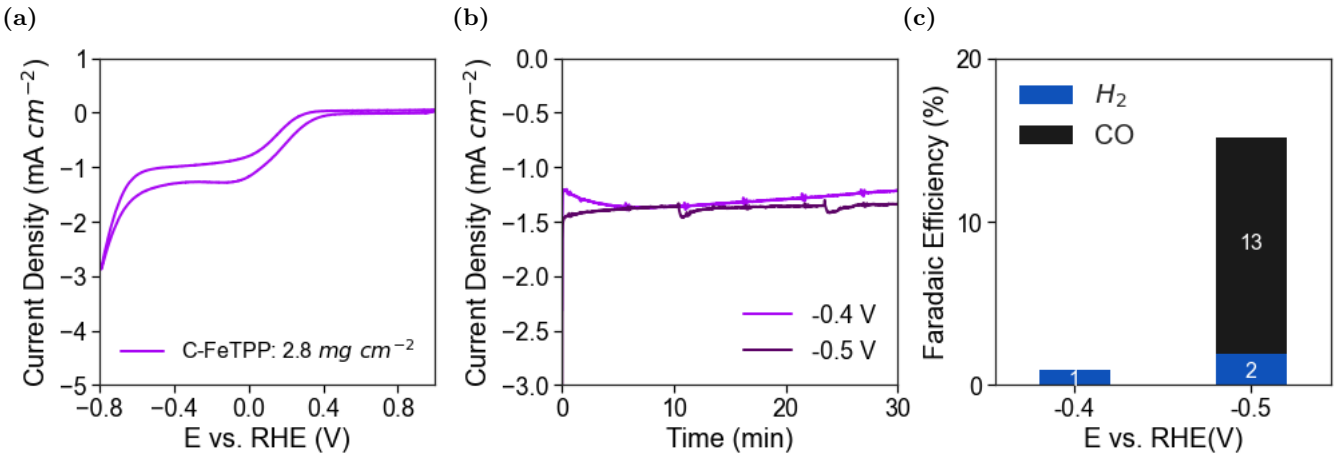

Figure A.5: Behaviour of FeTPP with a loading of 2.8 $mg\ cm^{-2}$ dropcasted on a C-GDE under CO_2 atmosphere. **a)** Cyclic Voltammetry. **b)** Chronoamperometry at different reductive potentials (V_{RHE}) and **c)** Faradaic efficiency for the chronoamperometry studies corresponding to b).

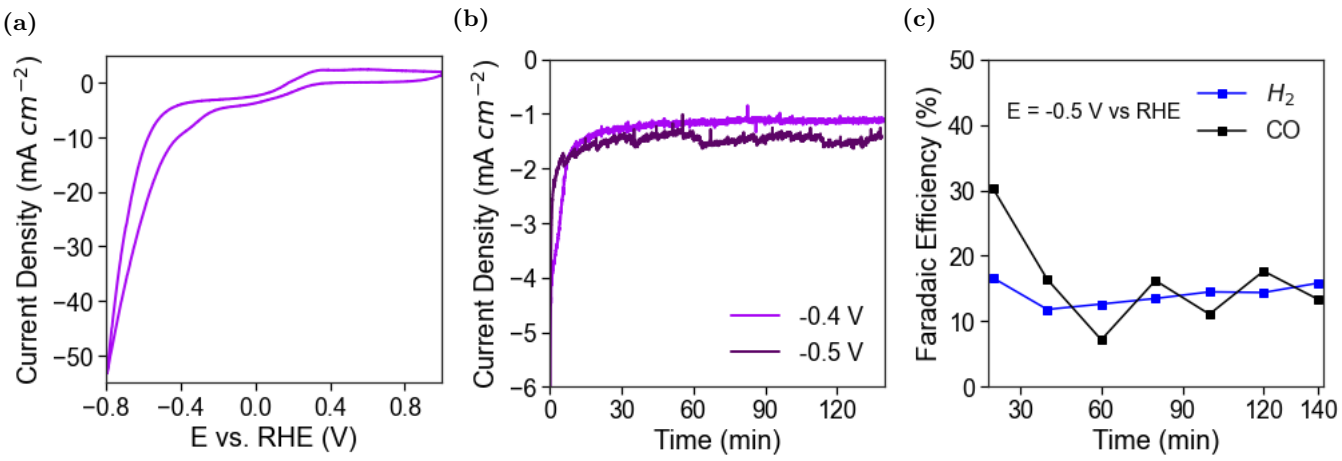

Figure A.6: 140 min run behaviour of FeTPP with a loading of 2.8 $mg\ cm^{-2}$ dropcasted on Ni Sputtered GDE under CO_2 atmosphere. **a)** Cyclic Voltammetry. **b)** Chronoamperometry at different reductive potentials (V_{RHE}) and **c)** Faradaic efficiency as a function of time.

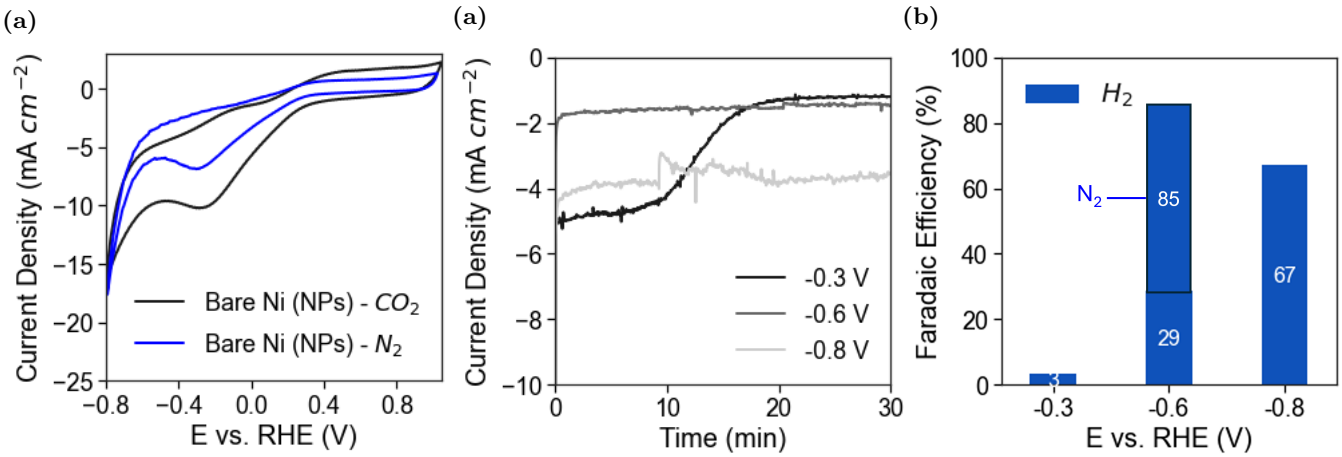

Figure A.7: Behaviour of Bare Ni NPs spray-coated on a C-GDE under CO_2 and N_2 atmospheres. **a)** Cyclic Voltammetry. **b)** Cronoamperometry studies under CO_2 at different reductive potentials, **c)** Faradaic efficiencies reached after 30 min of electrolysis under different reductive potentials on CO_2.

The CV curve of the spray-coated Ni-GDE (FigA.7a) is similar to that of the sputtered Ni-GDE (FigA.2a). However, the cathodic current is higher for the reduction of NiO_x and α-$Ni(OH)_2$ in the spray-deposited case, which we attribute to the thicker $1\ \mu m$ catalyst layer when compared to the 300 nm sputtered Ni-GDE. As Ni forms a thin NiO layer under ambient conditions it undergoes a $Ni^{2+/0}$ redox process during reductive polarization.[36] Overall, the expected HER activity under N_2 is higher than the CO_2 atmosphere, as explained for Fig.5a.

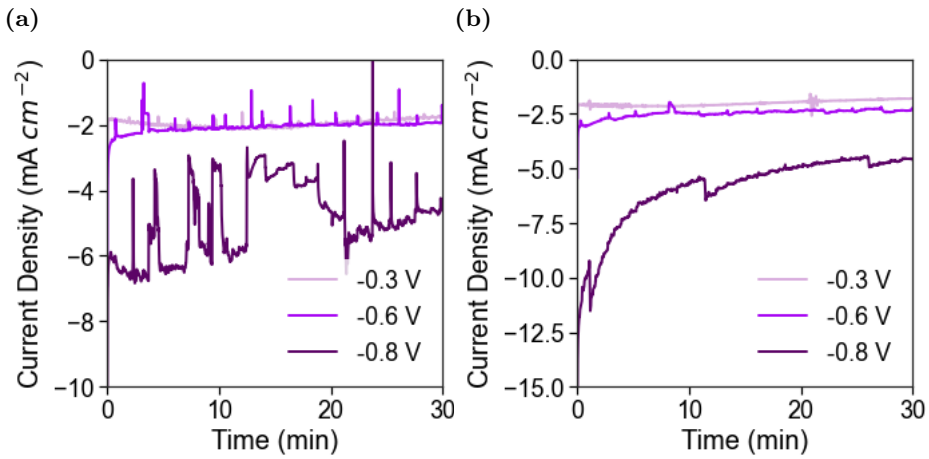

Figure A.8: Chronopotentiometry studies of different FeTPP coatings on Ni NPs spraycoated on a C-GDE under CO_2 atmosphere. **a)** One mono-layer, **b)** 40 FeTPP layers

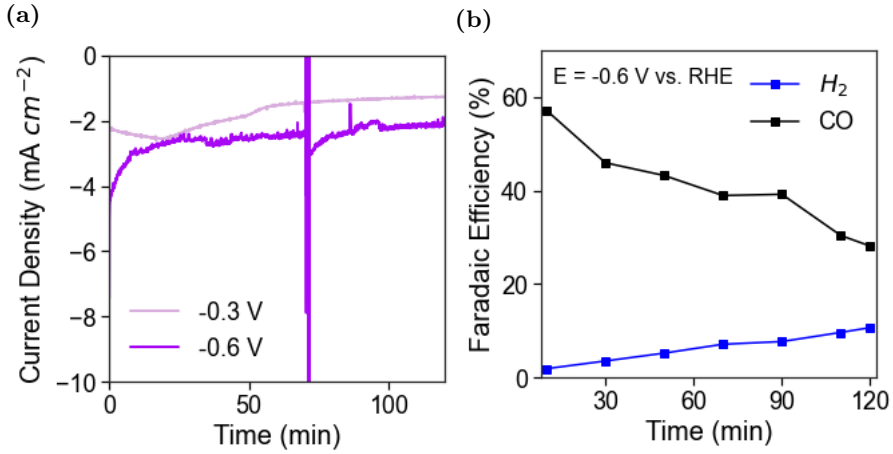

Figure A.9: 140 min run behaviour of 40 layers of FeTPP on Ni-NPs spray-coated on C-GDE under CO_2 atmosphere. a) Chronopotentiometry. **a)** Chronoamperometry at different reductive potentials (V_{RHE}) and **b)** Faradaic efficiency versus time for the chronoamperometry studies.

B.1 XRD and SEM Characterization

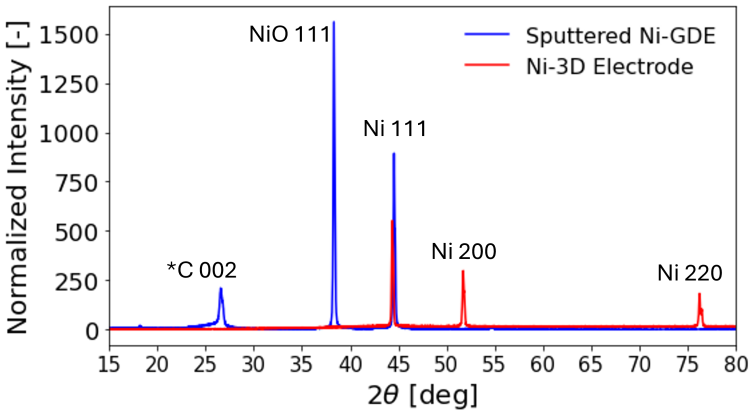

Figure A.10: X-ray diffraction patterns of our 300 *nm* sputtered Ni-GDE and the Ni 3D electrode. The peak identification was based on the study of Richardson *et al.*.[64]

The XRD patterns (A.10) reveal a sharp NiO peak (111) for our sputtered Ni-GDE compared to the 3D electrode. This is attributed to the facets of the crystal structure; our Ni-GDEs have increased surface area and smaller particle sizes, leading to a higher bulk concentration of NiO. In contrast, the Ni-3D electrode has a lower bulk concentration of NiO due to larger particle sizes, which limit the total bulk concentration of NiO.

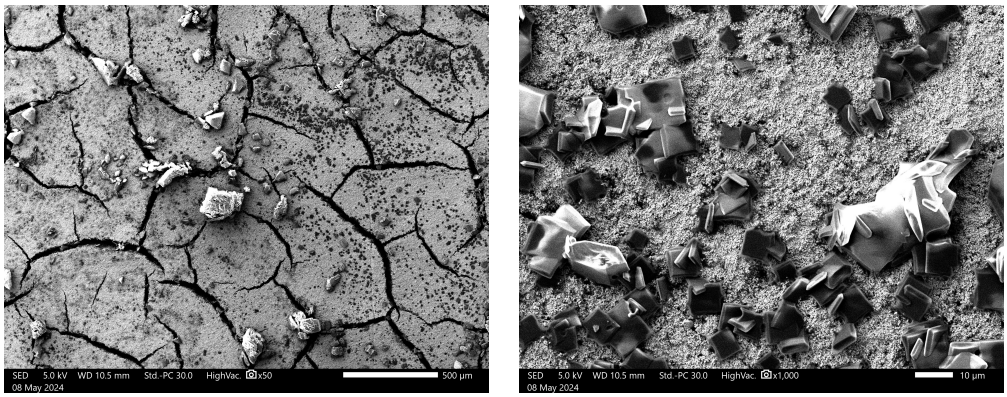

Figure A.11: SEM images of Ni-FeTPP dropcasted with a loading of 2.8 $mg\ cm^{-2}$

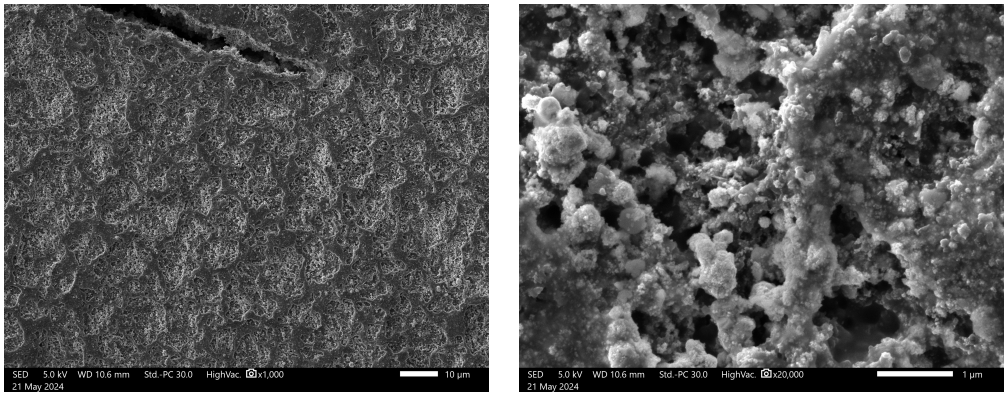

Figure A.12: SEM images of Ni nanoparticles with FeTPP mono-layer spray-coated on a carbon GDE

B.2 XPS Characterization

The following elemental composition was determined from the XPS measurements:

	C	O	Ni	Fe
Bare Sputtered Ni-GDE	23.68	41.65	34.67	0.00
FeTPP 2.8 $mg\ cm^{-2}$ on C-GDE	88.30	7.84	2.52	1.34
Ni NPs-FeTPP monolayer	67.54	25.29	7.16	0.16
Ni NPs-FeTPP *40 layers	81.50	12.53	5.97	0.21

Table 1: Elemental composition for different GDEs based on XPS survey.

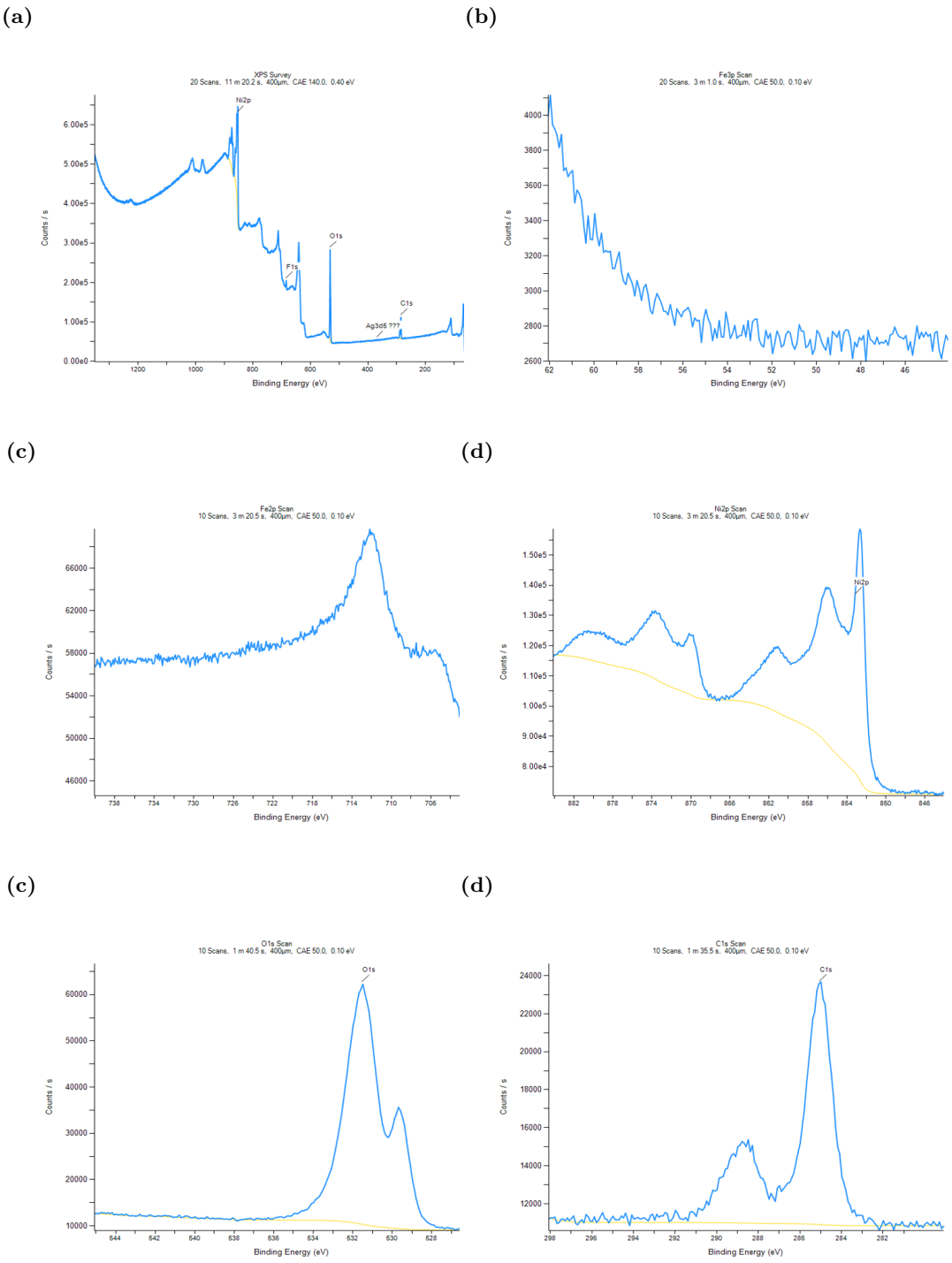

Figure A.13: XPS scans on the Bare sputtered Ni-GDE.

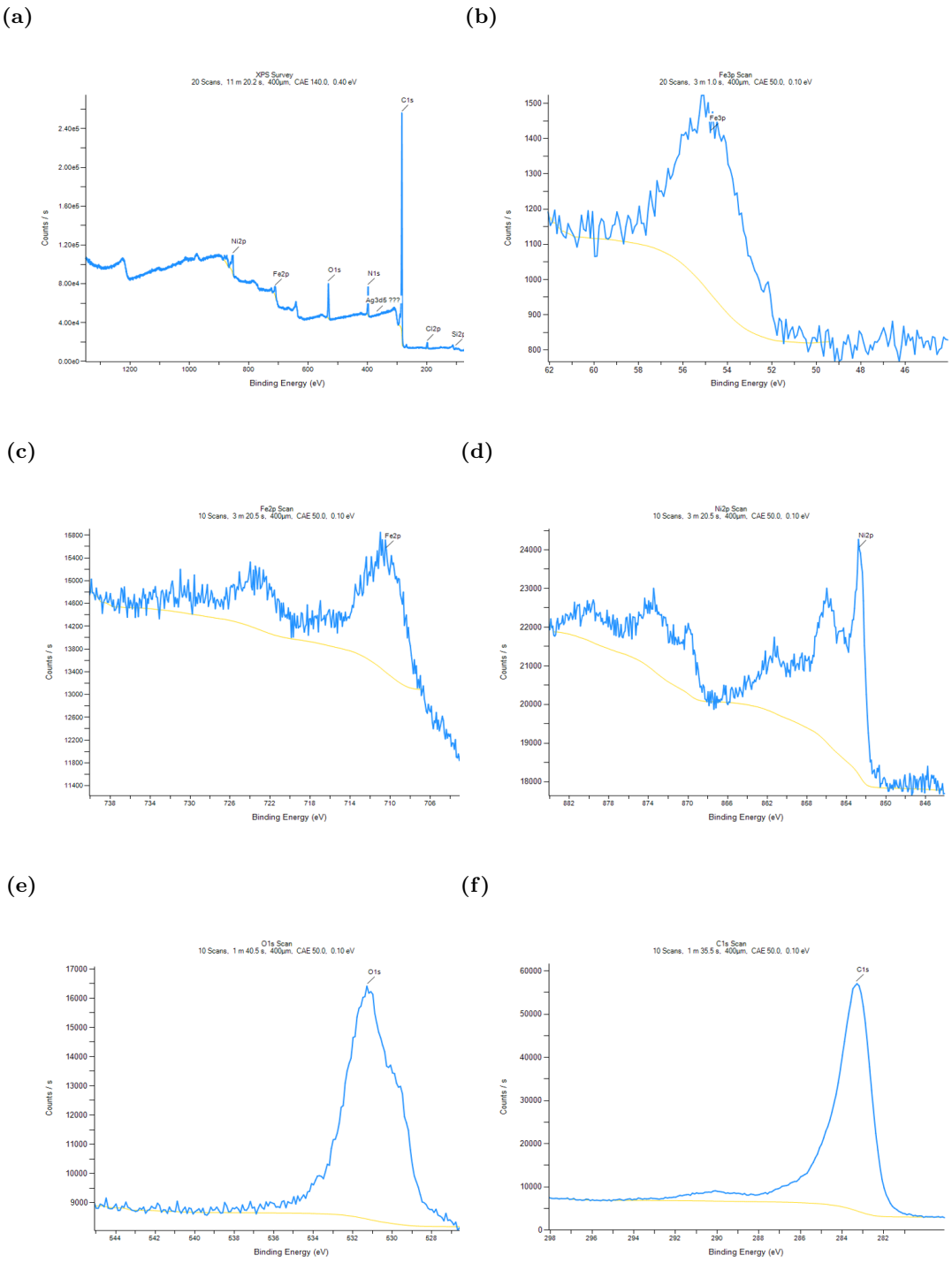

Figure A.14: XPS scans on the drop-casted FeTPP 2.8 $mg\ cm^{-2}$ on carbon GDE.

(a)

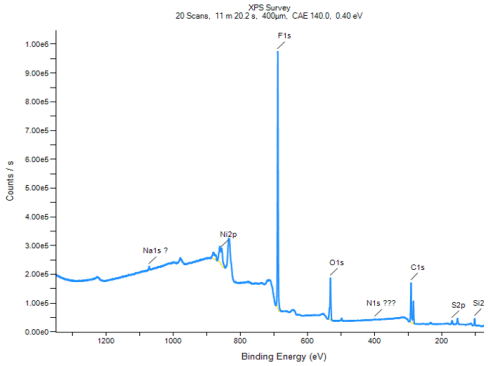

(b)

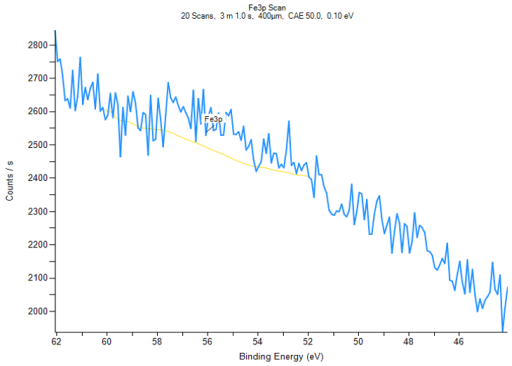

(c)

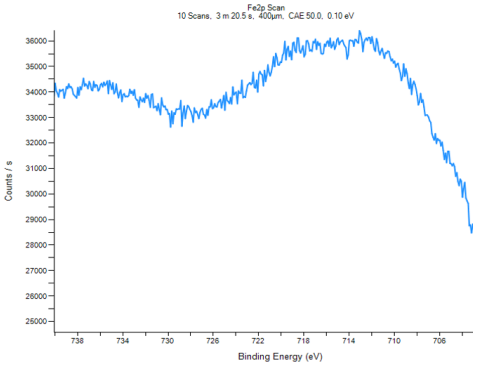

(d)

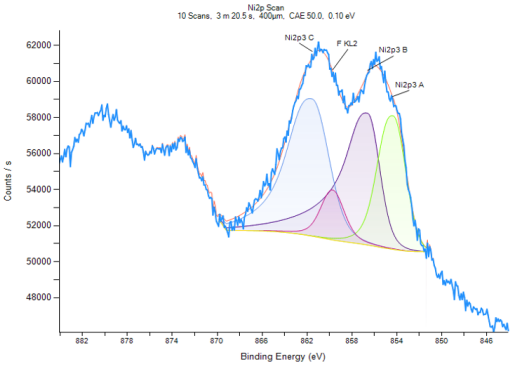

(e)

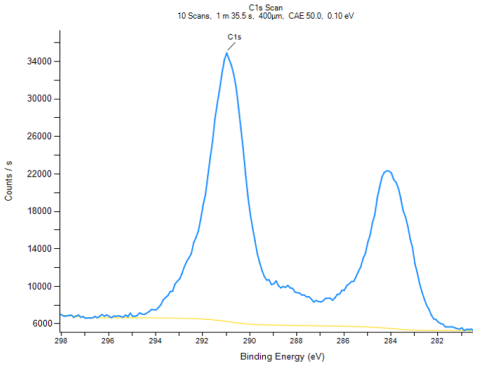

(f)

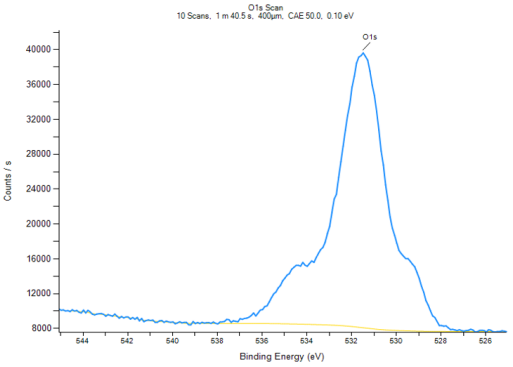

Figure A.15: XPS scans on a Ni NPs - FeTPP monolayer GDE.

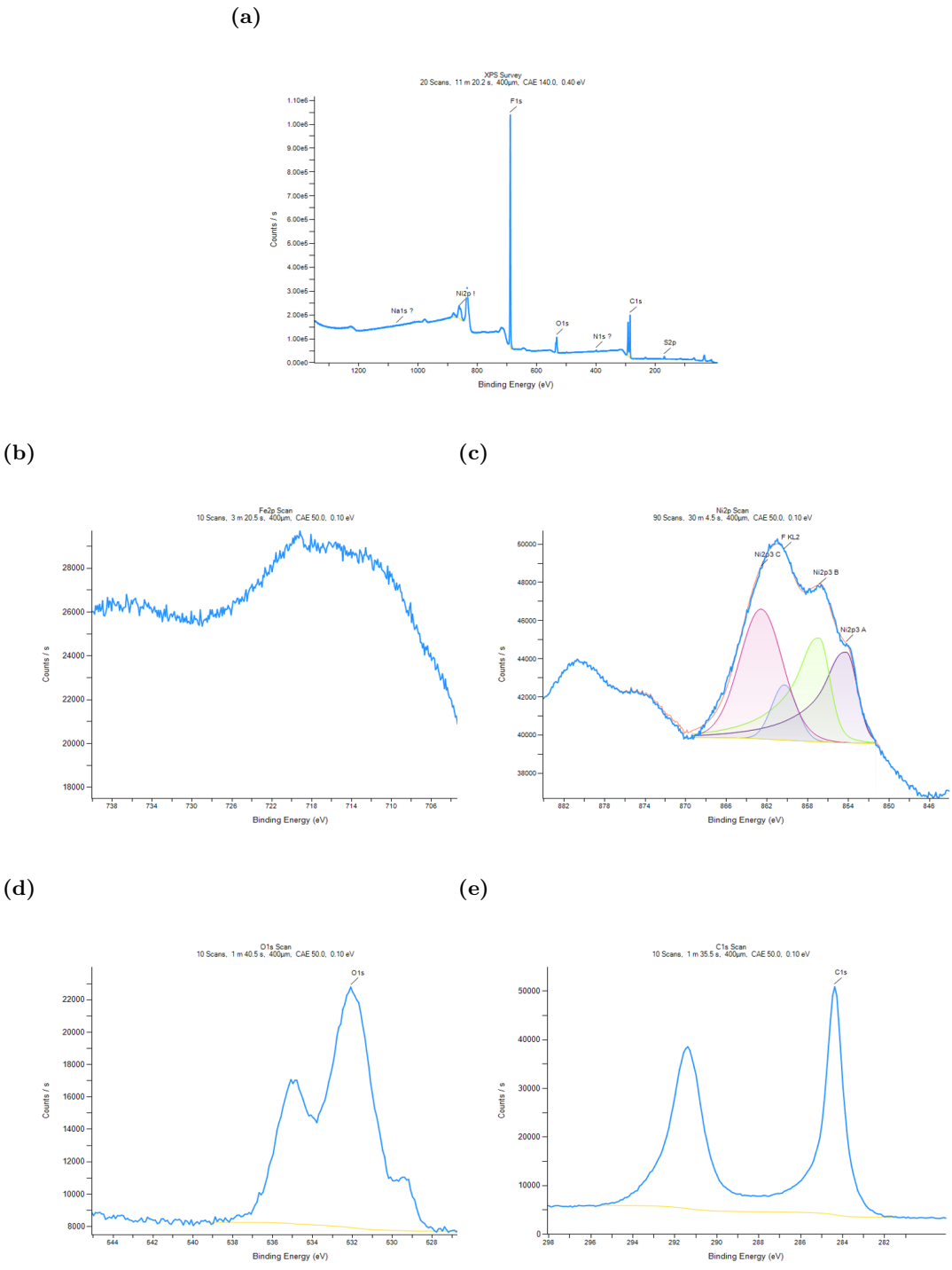

Figure A.16: XPS scans on a Ni NPs - FeTPP 40 layers GDE.

Nernst Equation relating the electrochemical potential and fugacity of H_2:

$$E = E^o - \frac{RT}{F} ln \left(\frac{\sqrt{f(\mathrm{H_2})/p^o}}{a(H^+)} \right) \tag{6}$$

Where E = potential (V), E^o = standard reversible potential (V), R = gas constant $J\ mol^{-1}\ K^{-1}$, T = temperature (K), F = Faraday constant, p^o = pressure (atm), and a(H^+) = protons activity. Adapted from Padavala and co-workers.[42]

B.3 Diffusion Model

$$\frac{dC}{dt} = D\frac{d^2C}{dx^2} \tag{7}$$

By implementing characteristic scales to the equation and applying $O(1)$ scaling to the time-dependent term and the diffusion term, and then rearranging the resulting equation, t_d can be calculated: Where:

- $C = H_{abs}$ concentration normalized [-]
- D = diffusion coefficient for H_{abs} in metallic Ni at 303.15 K= 5.6x10$^{-14} m^2\ s^{-1}$.[65]
- x = diameter of the Ni particle

By implementing the following scales to Eqn.1, we can determine t_d over a characteristic distance δ:

- $C^* = \frac{C}{[C]} = \frac{C}{C_0}$
- $x^* = \frac{x}{[x]} = \frac{x}{\delta}$
- $t^* = \frac{t}{[t]} = \frac{t}{t_d}$

Which results in:

$$\frac{C_0\ dC^*}{t_d\ dt^*} = D\frac{C_0\ d^2C^*}{\delta^2\ dx^{*2}} \tag{8}$$

Finally, by applying $O(1)$ scaling to the time-dependent term and the diffusion term, and then rearranging the resulting equation, t_d can be calculated:

$$\boxed{t_d = \frac{\delta^2}{D}} \tag{9}$$

$\boxed{t_{d-5\mu m} = 446\ s}$ vs. $\boxed{t_{d-100nm} = 0.18\ s}$

Semi-Infinite Diffusion Model: Assumes a constant concentration C_0 at the boundary of a finite diffusion region, extending infinitely into the surrounding medium.

Analytical Solution of Fick's Second Law:

The concentration profile $C(x,t)$ for this model is given by:

$$C(x,t) = C_0 \cdot \text{erfc}\left(\frac{x}{2\sqrt{Dt}}\right)$$

Where:

- $C(x,t)$ represents the concentration of the diffusing substance at position x and time t.
- C_0 is the initial concentration at the boundary.
- D is the diffusion coefficient.
- t is the time.
- erfc is the complementary error function, defined as $\text{erfc}(z) = 1 - \text{erf}(z)$, where $\text{erf}(z)$ is the error function.

Modeled by the following Python scripts:

```python
import numpy as np
import matplotlib.pyplot as plt
from scipy.special import erf


D = 5.6e-14 #m2/s
Co = 1  # Initial concentration [-]]
x1 = 5e-6/2  # Distance in meters (5um)

x3 = 100e-9/2  # Distance in meters (1000 nm)


# Time points
t_points = np.linspace(0,3600,1000)  # Time values (s)

# Analytical solution for concentration profile
def concentration_profile(x, t):
    return Co * (erf(x / (2 * np.sqrt(D * t))))

# Plot the concentration profiles
plt.figure(figsize=(4.5, 4.5))

# Plot for x1, x2, and x3
plt.plot(t_points/60, concentration_profile(x1, t_points), 'red', label=f"3D-E: 5 µm")
plt.plot(t_points/60, concentration_profile(x3, t_points),'blue', label=f"GDE: 100 nm")
plt.xlabel("time (min)",  color='black', fontsize = '20')
plt.ylabel("H$_{abs}$ [-]",  color='black', fontsize = '20')
plt.tick_params(axis='x', colors='black', labelsize=18)
plt.tick_params(axis='y', colors='black', labelsize=18)
plt.legend(title='', loc = 'best', edgecolor = 'None', fontsize = '18', labelcolor = 'black')


plt.tight_layout()
plt.show()


print('td_5 um = ', (x1**2/D), 'Seconds')
print('td_100nm = ', (x2**2/D), 'Seconds' )


import numpy as np
import matplotlib.pyplot as plt
from scipy.special import erf

D = 5.6e-14 #m^2/s (Diffusion Coefficient)
Co = 1  # Initial concentration normalized [-]
x1 = 5e-6  # Distance in meters (5um) for Ni 3D Electrode
x2 = 100e-9  # Distance in meters (100 nm) for Ni-GDE

t1 = x1**2/D #Characteristic time for Diffusion td (s) corresponding to x1
t2 = x2**2/D #Characteristic time for Diffusion td (s) corresponding to x1

#X domain
x_points = np.linspace(0 ,10e-9,1000000)  # X domain (um)

# Analytical solution for concentration profile
def concentration_profile(x, t):
    return Co * (1-erf(x / (2 * np.sqrt(D * t))))

# Plot for the concentration profiles as a function of X, given t
plt.figure(figsize=(4.9, 4.5))

plt.plot(x_points*1e9, concentration_profile(x_points, t1),'red', label=f"3D-E\nt$_d$ = 446 s")
plt.plot(x_points*1e9, concentration_profile(x_points, t2), 'blue', label=f"GDE\nt$_d$ = 0.18 s")
```

```
65
66  plt.xlabel("$\delta$ (nm)",  color='black', fontsize = '20')
67  plt.ylabel("H$_{abs}$ [-]",  color='black', fontsize = '20')
68  plt.tick_params(axis='x', colors='black', labelsize=18)
69  plt.tick_params(axis='y', colors='black', labelsize=18)
70  legend = plt.legend(title='', loc = 'best', edgecolor = 'None', fontsize = '16.5', labelcolor = 'black')
71  legend.set_frame_on(False)
72  #plt.xticks([0, 0.75, 1.5, 2.5], color='black', fontsize=18)
73
74  plt.tight_layout()
75  plt.show()
76
77
78  print('td_5 um = ', t1, 'Seconds')
79  print('td_100nm = ', t2, 'Seconds' )
```

C Local environment interaction

C.1 Theoretical CO_2 Conversion (X_{CO_2})

The theoretical current required to convert 100% of 5 sccm of CO_2 in 1 minute was calculated by using Faraday's Law:

$$Q = n\ F\ e$$

Where Q = number of charges (Coulombs), F = Faraday's constant = 96485 C/mol e, e = number of electrons used in electrochemical reaction (2 for CO_2-to-CO). A 50% factor of CO_2 lost in $KHCO_3$ was applied to convert the actual amount of CO_2 reacting.

- mol CO_2 = $\frac{\rho_{CO_2}}{M_{CO_2}}$
- 5 mL CO_2 x $\frac{0.00196g}{mL}$ = 0.0098 g CO_2 x $\frac{mol\ CO_2}{44.01\ g}$ = 2.27 x 10^{-4} mol CO_2
- Q = 2 x 2.27 x 10^{-4} x 96485 C/mol e x 2e = 42.9676 C/60 s = 0.716 Amperes x 0.5 (dilution factor) = 358 A
- Which divided by the working area of the electrode ($5cm^2$) = 358mA /$5cm^{-2}$ $\approx$ 72 $mA\ cm^{-2}$

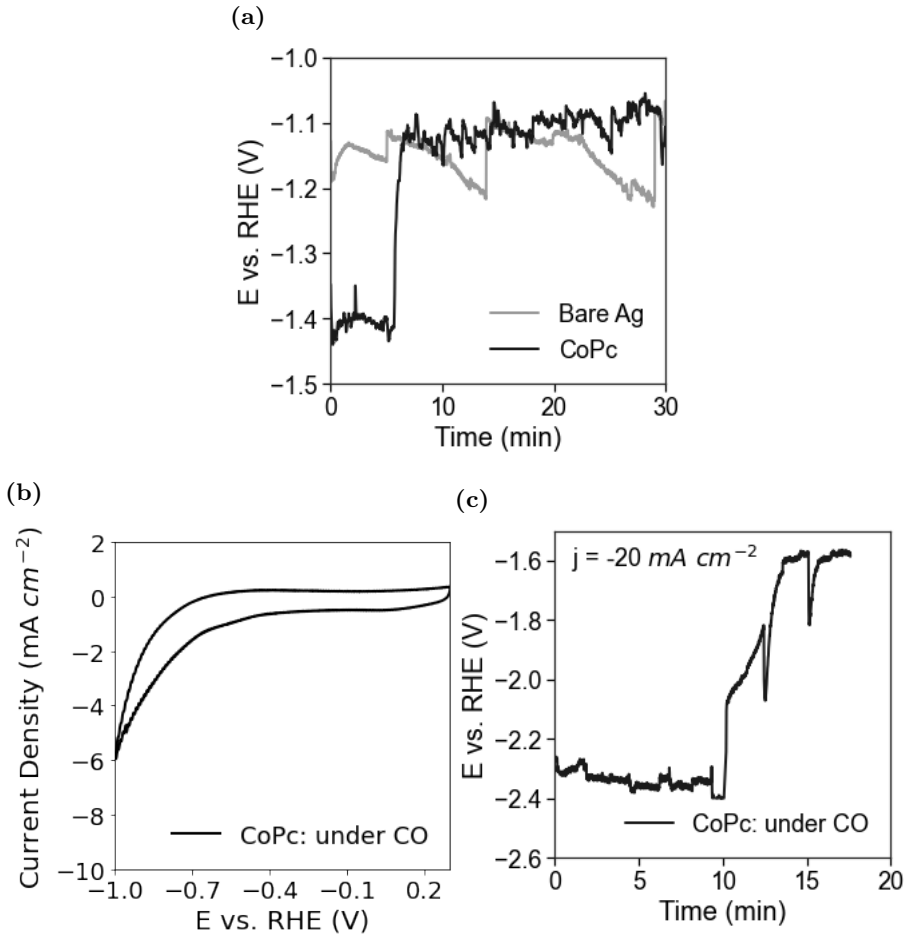

Figure A.17: Chronopotentiometry studies of **a)** Bare Ag (100 nm) sputtered on ePTFE under CO_2 atmosphere and CoPc 3 wt% spraycoated on Ag-ePTFE under CO_2, and **b)** CV of CoPc/MWCNT under CO atmosphere at a reductive current of -19 $mA\ cm^{-2}$, **c)** FE after 30 minutes of electrolysis reductive current of -19 $mA\ cm^{-2}$

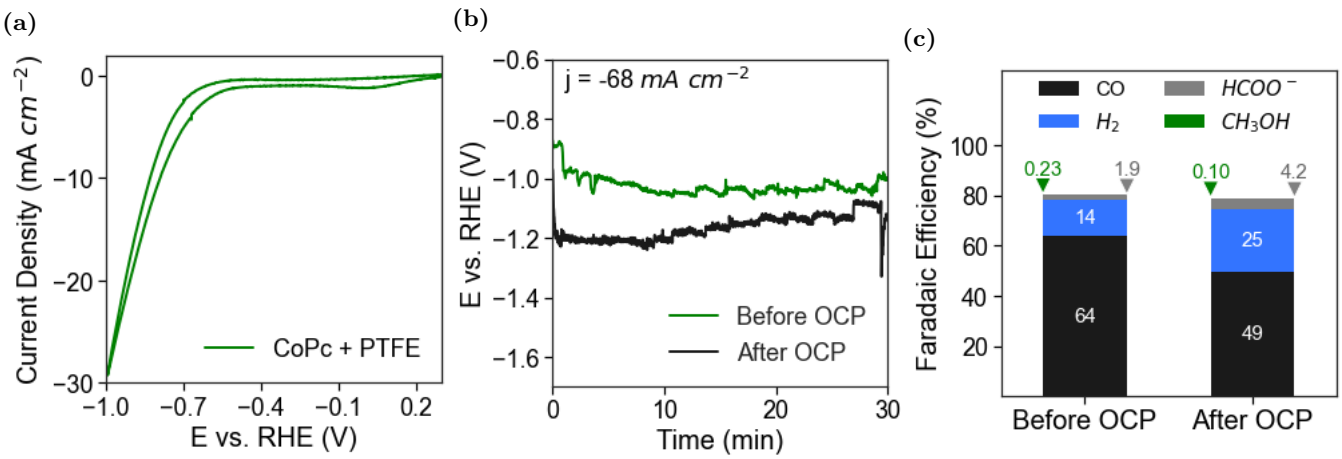

Figure A.18: Decrease in catalytic activity when going back to OCP for a CoPc 3wt% + PTFE electrode. **a)** Cyclic Voltammetry. **b)** Chronopotentiometry at a reductive current of -68 $mA\ cm^{-2}$ (V_{RHE}) and **c)** Faradaic efficiency after 30 min of chronopotentiometry before and after going back to OCP.

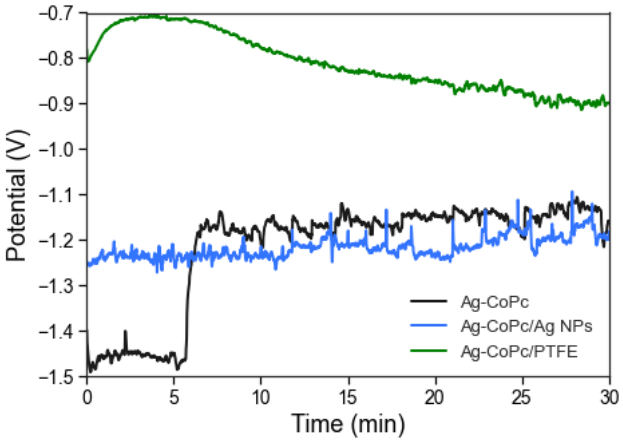

Figure A.19: Chronopotentiometry of different CoPc systems at a reductive current of -72 $mA\ cm^{-2}$

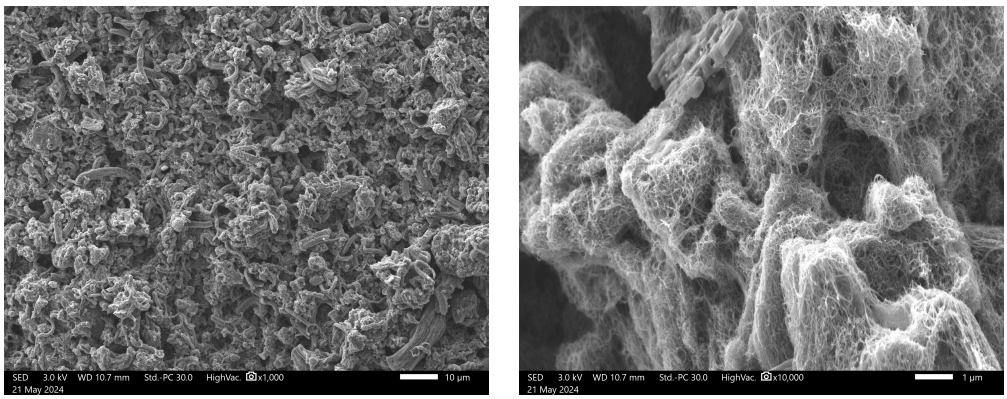

Figure A.20: SEM images of CoPc/MWCNT base-case GDE.

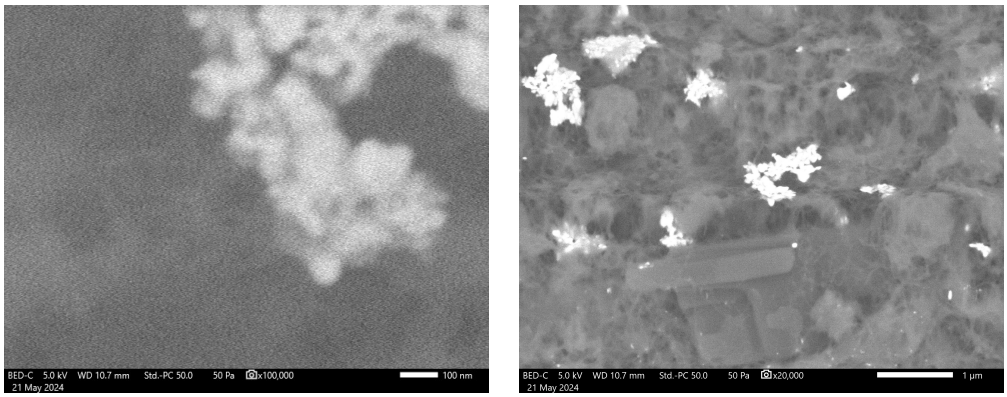

Figure A.21: SEM images of CoPc/MWCNT + Ag nanoparticles GDE.

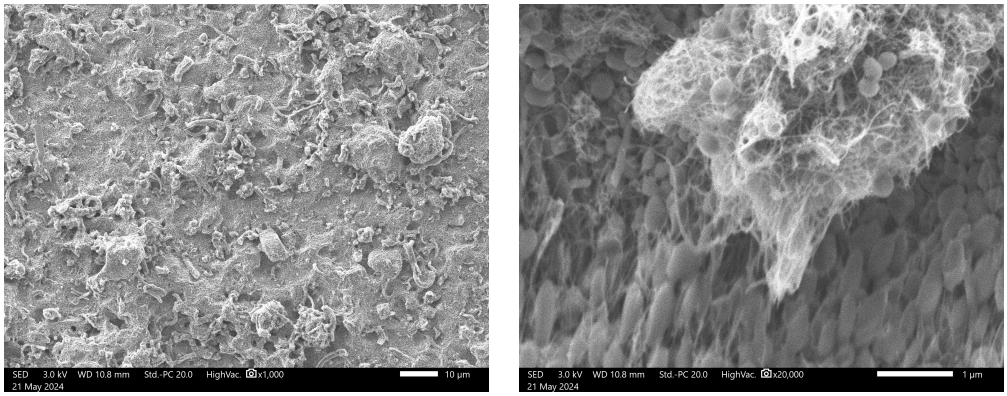

Figure A.22: SEM images of CoPc/MWCNT + PTFE particles GDE.

References

[1] Oleksandr S Bushuyev et al. "What should we make with CO2 and how can we make it?" In: *Joule* 2.5 (2018), pp. 825–832.

[2] Wilson A Smith et al. "Pathways to industrial-scale fuel out of thin air from CO2 electrolysis". In: *Joule* 3.8 (2019), pp. 1822–1834.

[3] Johan A Martens et al. "The chemical route to a carbon dioxide neutral world". In: *ChemSusChem* 10.6 (2017), pp. 1039–1055.

[4] Phil De Luna et al. "What would it take for renewably powered electrosynthesis to displace petrochemical processes?" In: *Science* 364.6438 (2019), eaav3506.

[5] Thomas Burdyny and Wilson A Smith. "CO 2 reduction on gas-diffusion electrodes and why catalytic performance must be assessed at commercially-relevant conditions". In: *Energy & Environmental Science* 12.5 (2019), pp. 1442–1453.

[6] Zhenyu Sun et al. "Fundamentals and challenges of electrochemical CO2 reduction using two-dimensional materials". In: *Chem* 3.4 (2017), pp. 560–587.

[7] Genxiang Wang et al. "Electrocatalysis for CO 2 conversion: from fundamentals to value-added products". In: *Chemical Society Reviews* 50.8 (2021), pp. 4993–5061.

[8] Libo Yao et al. "Challenges and Opportunities in Translating Immobilized Molecular Catalysts for Electrochemical CO2 Reduction from Aqueous-Phase Batch Cells to Gas-Fed Flow Electrolyzers". In: *Current Opinion in Electrochemistry* (2023), p. 101362.

[9] Hugo-Pieter Iglesias van Montfort et al. "An Advanced Guide to Assembly and Operation of CO2 Electrolyzers". In: *ACS Energy Letters* 8.10 (2023), pp. 4156–4161.

[10] Mark Sassenburg et al. "Characterizing CO2 reduction catalysts on gas diffusion electrodes: Comparing activity, selectivity, and stability of transition metal catalysts". In: *ACS Applied Energy Materials* 5.5 (2022), pp. 5983–5994.

[11] Abebe Reda Woldu et al. "Electrochemical CO2 reduction (CO2RR) to multi-carbon products over copper-based catalysts". In: *Coordination Chemistry Reviews* 454 (2022), p. 214340.

[12] Jinli Yu et al. "Recent progresses in electrochemical carbon dioxide reduction on copper-based catalysts toward multicarbon products". In: *Advanced Functional Materials* 31.37 (2021), p. 2102151.

[13] Domenico Grammatico et al. "Heterogenised molecular catalysts for sustainable electrochemical CO2 reduction". In: *Angewandte Chemie* 134.38 (2022), e202206399.

[14] Nathan T Nesbitt et al. "Liquid–solid boundaries dominate activity of CO2 reduction on gas-diffusion electrodes". In: *ACS Catalysis* 10.23 (2020), pp. 14093–14106.

[15] Robert Francke, Benjamin Schille, and Michael Roemelt. "Homogeneously catalyzed electroreduction of carbon dioxide—methods, mechanisms, and catalysts". In: *Chemical reviews* 118.9 (2018), pp. 4631–4701.

[16] Maryam Abdinejad, M Nur Hossain, and Heinz-Bernhard Kraatz. "Homogeneous and heterogeneous molecular catalysts for electrochemical reduction of carbon dioxide". In: *RSC advances* 10.62 (2020), pp. 38013–38023.

[17] Jiong Wang, Shuo Dou, and Xin Wang. "Structural tuning of heterogeneous molecular catalysts for electrochemical energy conversion". In: *Science Advances* 7.13 (2021), eabf3989.

[18] Corey J Kaminsky et al. "Adsorbed cobalt porphyrins act like metal surfaces in electrocatalysis". In: *Nature Catalysis* 5.5 (2022), pp. 430–442.

[19] Megan N Jackson et al. "Strong electronic coupling of molecular sites to graphitic electrodes via pyrazine conjugation". In: *Journal of the American Chemical Society* 140.3 (2018), pp. 1004–1010.

[20] Libo Sun et al. “Electrocatalytic reduction of carbon dioxide: opportunities with heterogeneous molecular catalysts”. In: *Energy & Environmental Science* 13.2 (2020), pp. 374–403.

[21] Nathan Corbin et al. “Heterogeneous molecular catalysts for electrocatalytic CO 2 reduction”. In: *Nano Research* 12 (2019), pp. 2093–2125.

[22] Etienne Boutin and Marc Robert. “Molecular electrochemical reduction of CO2 beyond two electrons”. In: *Trends in Chemistry* 3.5 (2021), pp. 359–372.

[23] Yueshen Wu et al. “Domino electroreduction of CO2 to methanol on a molecular catalyst”. In: *Nature* 575.7784 (2019), pp. 639–642.

[24] Fengwang Li et al. “Cooperative CO2-to-ethanol conversion via enriched intermediates at molecule–metal catalyst interfaces”. In: *Nature Catalysis* 3.1 (2020), pp. 75–82.

[25] Minghui Zhu et al. “Cobalt phthalocyanine coordinated to pyridine-functionalized carbon nanotubes with enhanced CO2 electroreduction”. In: *Applied Catalysis B: Environmental* 251 (2019), pp. 112–118.

[26] Xuefeng Wu et al. “Molecularly dispersed cobalt phthalocyanine mediates selective and durable CO2 reduction in a membrane flow cell”. In: *Advanced Functional Materials* 32.11 (2022), p. 2107301.

[27] Jianjun Su et al. “Strain enhances the activity of molecular electrocatalysts via carbon nanotube supports”. In: *Nature Catalysis* 6.9 (2023), pp. 818–828.

[28] Giulia Marcandalli et al. “Electrolyte effects on CO2 electrochemical reduction to CO”. In: *Accounts of chemical research* 55.14 (2022), pp. 1900–1911.

[29] Maryam Abdinejad et al. “Eliminating redox-mediated electron transfer mechanisms on molecular catalysts enables CO2 conversion to ethanol”. In: (2023).

[30] Peter T Smith et al. “Iron porphyrins embedded into a supramolecular porous organic cage for electrochemical CO2 reduction in water”. In: *Angewandte Chemie International Edition* 57.31 (2018), pp. 9684–9688.

[31] Yanbing Zhu et al. “Nickel-based electrodes as catalysts for hydrogen evolution reaction in alkaline media”. In: *Ionics* 24.4 (2018), pp. 1121–1127.

[32] Philipp Gotico et al. “Second-Sphere Biomimetic Multipoint Hydrogen-Bonding Patterns to Boost CO2 Reduction of Iron Porphyrins”. In: *Angewandte Chemie International Edition* 58.14 (2019), pp. 4504–4509.

[33] Cyrille Costentin, Marc Robert, and Jean-Michel Saveant. “Current issues in molecular catalysis illustrated by iron porphyrins as catalysts of the CO2-to-CO electrochemical conversion”. In: *Accounts of chemical research* 48.12 (2015), pp. 2996–3006.

[34] Shaoxuan Ren et al. “Catalyst aggregation matters for immobilized molecular CO2RR electrocatalysts”. In: *Journal of the American Chemical Society* 145.8 (2023), pp. 4414–4420.

[35] Eric W Lees et al. “Linking gas diffusion electrode composition to CO 2 reduction in a flow cell”. In: *Journal of Materials Chemistry A* 8.37 (2020), pp. 19493–19501.

[36] Y Unutulmazsoy et al. “The oxidation kinetics of thin nickel films between 250 and 500 C”. In: *Physical Chemistry Chemical Physics* 19.13 (2017), pp. 9045–9052.

[37] Yoshio Hori and Akira Murata. “Electrochemical evidence of intermediate formation of adsorbed CO in cathodic reduction of CO2 at a nickel electrode”. In: *Electrochimica Acta* 35.11-12 (1990), pp. 1777–1780.

[38] Yoshio Hori et al. “Infrared spectroscopic observation of adsorbed CO intermediately formed in the electrochemical reduction of CO2 at a nickel electrode”. In: *Bulletin of the Chemical Society of Japan* 65.11 (1992), pp. 3008–3010.

[39] Alexander Bagger et al. “Electrochemical CO2 reduction: a classification problem”. In: *ChemPhysChem* 18.22 (2017), pp. 3266–3273.

[40] Rafaël E Vos and Marc TM Koper. "Nickel as Electrocatalyst for CO (2) Reduction: Effect of Temperature, Potential, Partial Pressure, and Electrolyte Composition". In: *ACS catalysis* 14.7 (2024), pp. 4432–4440.

[41] Kendra P Kuhl et al. "Electrocatalytic conversion of carbon dioxide to methane and methanol on transition metal surfaces". In: *Journal of the American Chemical Society* 136.40 (2014), pp. 14107–14113.

[42] Sri Krishna Murthy Padavala and Kelsey A Stoerzinger. "Role of hydride formation in electrocatalysis for sustainable chemical transformations". In: *ACS Catalysis* 13.7 (2023), pp. 4544–4551.

[43] DM Soares, O Teschke, and I. Torriani. "Hydride Effect on the Kinetics of the Hydrogen Evolution Reaction on Nickel Cathodes in Alkaline Media". In: *J. Electrochem. Soc* (1992).

[44] Martijn JW Blom et al. "Mechanism and micro kinetic model for electroreduction of CO2 on Pd/C: the role of different palladium hydride phases". In: *ACS catalysis* 11.12 (2021), pp. 6883–6891.

[45] Wenchao Sheng et al. "Electrochemical reduction of CO 2 to synthesis gas with controlled CO/H 2 ratios". In: *Energy & Environmental Science* 10.5 (2017), pp. 1180–1185.

[46] Xiao Zhou, Normand Mousseau, and Jun Song. "Is hydrogen diffusion along grain boundaries fast or slow? Atomistic origin and mechanistic modeling". In: *Physical review letters* 122.21 (2019), p. 215501.

[47] W.M. Deen. *Analysis of Transport Phenomena*. Topics in chemical engineering. Oxford University Press, 2012. ISBN: 9780199740284. URL: https://books.google.nl/books?id=60YsAwEACAAJ.

[48] Ahmed M Abdellah et al. "Impact of palladium/palladium hydride conversion on electrochemical CO2 reduction via in-situ transmission electron microscopy and diffraction". In: *Nature Communications* 15.1 (2024), p. 938.

[49] Maoyu Wang et al. "In situ X-ray absorption spectroscopy studies of nanoscale electrocatalysts". In: *Nano-Micro Letters* 11 (2019), pp. 1–18.

[50] Xinyi Ren et al. "In-situ spectroscopic probe of the intrinsic structure feature of single-atom center in electrochemical CO/CO2 reduction to methanol". In: *Nature Communications* 14.1 (2023), p. 3401.

[51] Libo Yao et al. "Electrochemical CO2 Reduction to Methanol by Cobalt Phthalocyanine: Quantifying CO2 and CO Binding Strengths and Their Influence on Methanol Production". In: *ACS Catalysis* 14.1 (2023), pp. 366–372.

[52] Hugo-Pieter Iglesias van Montfort et al. "Non-invasive current collectors for improved current-density distribution during CO2 electrolysis on super-hydrophobic electrodes". In: *Nature Communications* 14.1 (2023), p. 6579.

[53] Tu N Nguyen and Cao-Thang Dinh. "Gas diffusion electrode design for electrochemical carbon dioxide reduction". In: *Chemical Society Reviews* 49.21 (2020), pp. 7488–7504.

[54] Miguel Duarte et al. "Electrochemical reduction of CO2: effect of convective CO2 supply in gas diffusion electrodes". In: *ChemElectroChem* 6.22 (2019), pp. 5596–5602.

[55] Zhuo Xing et al. "Enhancing carbon dioxide gas-diffusion electrolysis by creating a hydrophobic catalyst microenvironment". In: *Nature communications* 12.1 (2021), p. 136.

[56] Ying Chuan Tan et al. "Modulating local CO2 concentration as a general strategy for enhancing C- C coupling in CO2 electroreduction". In: *Joule* 4.5 (2020), pp. 1104–1120.

[57] Dulce M Morales and Marcel Risch. "Seven steps to reliable cyclic voltammetry measurements for the determination of double layer capacitance". In: *Journal of Physics: Energy* 3.3 (2021), p. 034013.

[58] Md Mijanur Rahman et al. “Synthesis of catalysts with fine platinum particles supported by high-surface-area activated carbons and optimization of their catalytic activities for polymer electrolyte fuel cells”. In: *RSC advances* 11.33 (2021), pp. 20601–20611.

[59] Dianne Wiley and Gustavo Fimbres Weihs. “Electroosmotic Drag in Membranes”. In: *Encyclopedia of Membranes*. Ed. by Enrico Drioli and Lidietta Giorno. Berlin, Heidelberg: Springer Berlin Heidelberg, 2016, pp. 653–654. ISBN: 978-3-662-44324-8. DOI: 10.1007/978-3-662-44324-8_2078. URL: https://doi.org/10.1007/978-3-662-44324-8_2078.

[60] Faezeh Habibzadeh et al. “Ion exchange membranes in electrochemical CO2 reduction processes”. In: *Electrochemical Energy Reviews* 6.1 (2023), p. 26.

[61] Kristian Torbensen et al. “Iron porphyrin allows fast and selective electrocatalytic conversion of CO2 to CO in a flow cell”. In: *Chemistry–A European Journal* 26.14 (2020), pp. 3034–3038.

[62] Sergio Antonio Spinola Machado and Luís Alberto Avaca. “The hydrogen evolution reaction on nickel surfaces stabilized by H-absorption”. In: *Electrochimica acta* 39.10 (1994), pp. 1385–1391.

[63] Yoshio Hori et al. “Electrocatalytic process of CO selectivity in electrochemical reduction of CO2 at metal electrodes in aqueous media”. In: *Electrochimica Acta* 39.11-12 (1994), pp. 1833–1839.

[64] James T Richardson, Robert Scates, and Martyn V Twigg. “X-ray diffraction study of nickel oxide reduction by hydrogen”. In: *Applied Catalysis A: General* 246.1 (2003), pp. 137–150.

[65] J Li et al. “Anisotropy of hydrogen diffusion in nickel single crystals: the effects of self-stress and hydrogen concentration on diffusion”. In: *Scientific Reports* 7.1 (2017), p. 45041.